

¹ **Searches for Supersymmetry using the α_T**
² **variable with the CMS detector at the LHC**

³ Darren Burton

⁴ Imperial College London
⁵ Department of Physics

⁶ A thesis submitted to Imperial College London
⁷ for the degree of Doctor of Philosophy

Abstract

10

Declaration

11

I, the author of this thesis, declare that the work presented within this
12 document to be my own. The work presented in Chapters 3.4.1, 4 and 5
13 is a result of the authors own work or that of which I have been a major
14 contributor unless explicitly stated otherwise, and is carried out within the
15 context of the Imperial College London and CERN SUSY groups, itself a
16 subsection of the greater CMS collaboration. All figures and studies taken
17 from external sources are referenced appropriately throughout this document.

18

Darren Burton

19

Acknowledgements

20

Of the many people who deserve thanks, some are particularly prominent....

Preface

Contents

23	List of Figures	viii
24	List of Tables	xii
25	1. Introduction	2
26	2. A Theoretical Overview	5
27	2.1. The Standard Model	5
28	2.1.1. Gauge Symmetries of the SM	7
29	2.1.2. The Electroweak Sector and Electroweak Symmetry Breaking	9
30	2.2. Motivation for Physics Beyond the Standard Model	13
31	2.3. Supersymmetry Overview	15
32	2.3.1. R-Parity	16
33	2.4. Experimental signatures of SUSY at the LHC	17
34	2.4.1. Simplified Models	18
35	3. The LHC and the CMS Detector	20
36	3.1. The LHC	20
37	3.2. The CMS detector	23
38	3.2.1. Detector Subsystems	23
39	3.2.2. Tracker	24
40	3.2.3. Electromagnetic Calorimeter	25
41	3.2.4. Hadronic Calorimeter	26
42	3.2.5. Muon Systems	27
43	3.3. Event Reconstruction and Object Definition	28
44	3.3.1. Jets	28
45	3.3.2. B-tagging	30
46	3.4. Triggering System	32
47	3.4.1. The Level-1 Trigger	34

48	3.4.2. L1 Trigger Jet Algorithm	35
49	3.4.3. Measuring L1 Jet Trigger Efficiencies	36
50	3.4.4. Effects of the L1 Jet Seed	38
51	3.4.5. Robustness of L1 Jet Performance against Pile-up	41
52	3.4.6. Summary	43
53	4. SUSY searches in Hadronic Final States	45
54	4.1. An introduction to the α_T search	46
55	4.1.1. The α_T variable	48
56	4.2. Search Strategy	50
57	4.2.1. Control Sample Definition	52
58	4.3. Trigger Strategy	54
59	4.4. Event Selection	54
60	4.5. A method to determine MC yields with higher statistical precision	54
61	4.6. Systematic Uncertainties on Transfer Factors	54
62	4.7. Searches for Natural SUSY with B-tag templates.	54
63	5. Results	55
64	5.1. Statistical Interpretation	55
65	5.2. Interpretation in Simplified Signal Models	55
66	A. Miscellaneous	56
67	A.1. Noise Filters	56
68	A.2. Primary Vertices	57
69	B. L1 Jets	58
70	B.1. Jet matching efficiencies	58
71	B.2. Leading Jet Energy Resolution	59
72	B.3. Resolution for Energy Sum Quantities	62
73	Bibliography	68

⁷⁴ List of Figures

⁷⁵ 2.1.	One loop quantum corrections to the Higgs squared mass parameter m_h^2 due to a fermion.	⁷⁶ 14
⁷⁷ 2.2.	Two example simplified model decay chains.	⁷⁷ 19
⁷⁸ 3.1.	A top down layout of the LHC, with the position of the four main detectors labelled.	⁷⁹ 21
⁸⁰ 3.2.	The total integrated luminosity delivered to and collected by Compact Muon Solenoid (CMS) during the 2012 8 TeV pp runs	⁸¹ 22
⁸² 3.3.	A pictorial depiction of the CMS detector.	⁸³ 24
⁸³ 3.4.	Illustration of the CMS Electromagnetic CALorimeter (ECAL).	⁸⁴ 26
⁸⁴ 3.5.	Schematic of the CMS Hadronic CALorimeter (HCAL).	⁸⁵ 27
⁸⁵ 3.6.	Combined Secondary Vertex (CSV) algorithm discriminator values in enriched $t\bar{t}$ and inclusive multi jet samples	⁸⁶ 31
⁸⁷ 3.7.	Data/MC b-tag scale factors derived using the Combined Secondary Vertex Medium Working Point (CSVM) tagger.	⁸⁸ 32
⁸⁹ 3.8.	Data/MC mis-tag scale factors derived using the CSVM tagger.	⁹⁰ 33
⁹⁰ 3.9.	The CMS Level 1 Trigger (L1) Trigger system.	⁹¹ 34
⁹¹ 3.10.	Illustration of the Level-1 jet finding algorithm.	⁹² 36
⁹² 3.11.	L1 jet efficiency turn-on curves as a function of the offline CaloJet and PFJet E_T	⁹³ 38
⁹⁴ 3.12.	L1 jet efficiency turn-on curves as a function of the offline CaloJet E_T for the 2012 run period B and C.	⁹⁵ 39

96	3.13. Trigger cross section for the L1HTT150 trigger path.	40
97	3.14. L1 H_T efficiency turn-on curves as a function of the offline CaloJet H_T	41
98	3.15. L1 jet efficiency turn-on curves as a function of the leading offline E_T Calo (left) and PF (right) jet, for low, medium and high pile-up conditions.	42
100	3.16. Fit values from an Exponentially Modified Gaussian (EMG) function fitted to the resolution plots of leading Calo jet E_T measured as a function of $\frac{(L1\ E_T - \text{Offline}\ E_T)}{\text{Offline}\ E_T}$ for low, medium and high pile-up conditions.	43
103	3.17. Fit values from an EMG function fitted to the resolution plots of leading PF jet E_T measured as a function of $\frac{(L1\ E_T - \text{Offline}\ E_T)}{\text{Offline}\ E_T}$ for low, medium and high pile-up conditions.	44
106	4.1. Reconstructed offline H_T for 11.7fb^{-1} of data after a basic pre-selection.	48
107	4.2. The event topologies of background QCD dijet events (right) and a generic SUperSYmmetry (SUSY) signature with genuine \cancel{E}_T (left).	48
109	4.3. The α_T distributions for the low 2-3 (left) and high ≥ 4 (right) jet multiplicities after a full analysis selection and shown for $H_T > 375$	50
111	4.4. Pictorial depiction of the analysis strategy employed by the α_T search to increase sensitivity to a wide spectra of SUSY models.	53
113	B.1. Leading jet matching efficiency as a function of the offline CaloJet E_T	58
114	B.2. Resolution plots of the leading offline Calo E_T measured as a function of $\frac{(L1\ E_T - \text{Offline}\ E_T)}{\text{Offline}\ E_T}$ for low (a), medium (b) and high (c) pile-up conditions.	60
116	B.3. Resolution plots of the leading off-line PF E_T measured as a function of $\frac{(L1\ E_T - \text{Offline}\ E_T)}{\text{Offline}\ E_T}$ for low (a), medium (b) and high (c) pile-up conditions.	62
118	B.4. $\sum E_T$ resolution parameters in bins of Calo $\sum E_T$ measured for the defined low, medium and high pile up conditions.	63
120	B.5. $\sum E_T$ resolution parameters in bins of PF $\sum E_T$ measured for the defined low, medium and high pile up conditions.	63
122	B.6. \cancel{E}_T resolution parameters in bins of Calo \cancel{E}_T measured for the defined low, medium and high pile up conditions.	64

124	B.7. \cancel{E}_T resolution parameters in bins of PF \cancel{E}_T measured for the defined low,	
125	medium and high pile up conditions.	64
126	B.8. H_T resolution parameters in bins of Calo H_T measured for the defined	
127	low, medium and high pile up conditions.	65
128	B.9. H_T resolution parameters in bins of PF H_T measured for the defined low,	
129	medium and high pile up conditions.	65
130	B.10. \cancel{H}_T resolution parameters in bins of \cancel{H}_T measured for the defined low,	
131	medium and high pile up conditions.	66
132	B.11. \cancel{H}_T resolution parameters in bins of PF \cancel{H}_T measured for the defined low,	
133	medium and high pile up conditions.	66

¹³⁴ List of Tables

¹³⁵	2.1. The fundamental particles of the Standard Model (SM), with spin, charge and mass displayed.	6
¹³⁷	3.1. Results of a cumulative EMG function fit to the turn-on curves for L1 single jet triggers in 2012 Run Period C.	38
¹³⁹	3.2. Results of a cumulative EMG function fit to the turn-on curves for L1 single jet triggers in the 2012 run period B and C.	39
¹⁴¹	3.3. Results of a cumulative EMG function fit to the turn-on curves for H_T in 2012 run period B and C.	40
¹⁴³	3.4. Results of a cumulative EMG function fit to the efficiency turn-on curves for L1 single jet triggers in the 2012 run period C, for low,medium and high pile-up conditions.	41
¹⁴⁶	3.5. Results of a cumulative EMG function fit to the efficiency turn-on curves for Level-1 single jet triggers in the 2012 run period C, for low,medium and high pile-up conditions.	42
¹⁴⁹	4.1. A summary of the Simplified Model Spectra (SMS) models interpreted in this analysis, involving both direct (D) and gluino-induced (G) production of squarks and their decays.	46
¹⁵²	B.1. Results of a cumulative EMG function fit to the turn-on curves for the matching efficiency of the leading jet in an event to a Level-1 jet in run 2012C and 2012B data.	59

“The Universe is about 1,000,000 years old.”

— Matthew Kenzie, 1987-present : Discoverer of the Higgs Boson.

Chapter 1.

¹⁵⁷ Introduction

¹⁵⁸ During the 20th century great advances have been made in our understanding of the
¹⁵⁹ universe, where it comes from, where it is going and what it is made of. The Standard
¹⁶⁰ Model (**SM**) first formulated in the 1960's is one of the crowning achievements in science's
¹⁶¹ quest to explain the most fundamental processes and interactions that make up our
¹⁶² universe. It has provided a highly successful explanation of a wide range of phenomena
¹⁶³ in Particle Physics and has stood up to extensive experimental scrutiny [1].

¹⁶⁴ Despite it's successes it is not a complete theory, with significant questions remaining
¹⁶⁵ unanswered. It describes only three of the four known forces with gravity not incorpo-
¹⁶⁶ rated within the framework of the **SM**. Cosmological experiments infer that just $\sim 4\%$
¹⁶⁷ of the observable universe exists as matter, with elusive "Dark Matter" accounting for a
¹⁶⁸ further $\sim 23\%$ [2]. However no particle predicted by the **SM** is able to account for it. At
¹⁶⁹ higher energy scales and small distances the (non-)unification of the fundamental forces
¹⁷⁰ point to problems with the **SM** at least at higher energies not yet probed experimentally.

¹⁷¹ Many theories exist as extensions to the **SM** and predict a range of observables
¹⁷² that can be detected at the Large Hadron Collider (**LHC**) of which SUperSYmmetry
¹⁷³ (**SUSY**) is one such example. It predicts a new symmetry of nature in which all current
¹⁷⁴ particles in the **SM** would have a corresponding supersymmetric partner. Common to
¹⁷⁵ most Supersymmetric theories is a stable, weakly interacting Lightest Supersymmetric
¹⁷⁶ Partner (**LSP**), which has the properties of a possible dark matter candidate. The **SM**
¹⁷⁷ and the main principles of Supersymmetric theories are outlined in Chapter 2, with
¹⁷⁸ emphasis placed on how experimental signatures of **SUSY** may reveal themselves at
¹⁷⁹ the **LHC**.

180 The experimental goal of the **LHC** is to further test the framework of the **SM**,
181 exploring the TeV mass scale for the first time, and to seek a connection between the
182 particles produced in proton collisions and dark matter. The first new discovery by
183 this extraordinary machine was announced on the 4th of July 2012. The long-awaited
184 discovery was the culmination decades of experimental endeavours in the search for the
185 Higgs boson, providing an answer to the mechanism of electroweak symmetry breaking
186 within the **SM** [3][4].

187 This discovery was made possible through data taken by the two multi purpose
188 detectors (**CMS** and A Toroidal LHC Apparatus (**ATLAS**)) located on the **LHC** ring.
189 An experimental description of the **CMS** detector and the **LHC** is described in Chapter 3,
190 including some of the object reconstruction used by **CMS** in searches for **SUSY** signatures.
191 The performance of the **CMS** Level-1 calorimeter trigger, benchmarked by the author is
192 also included within this chapter.

193 The analysis conducted by the author is detailed within Chapter 4. This chapter
194 contains a description of the search for evidence of the production of Supersymmetric
195 particles at the **LHC**. The main basis of the search centres around the kinematic
196 dimensionless α_T variable, which provides strong rejection of backgrounds with fake
197 missing energy signatures whilst maintaining good sensitivity to a variety of **SUSY**
198 topologies. The author's work as an integral part of the analysis group is documented in
199 detail, which has culminated in numerous publications over the past two years. The latest
200 of which was published in the European Physical Journal C (**EPJC**) [5] and contains the
201 results which are discussed within this and the sequential Chapter.

202 The author in particular has played a major role in the extension of the α_T analysis into
203 the additional b-tagged and jet multiplicity dimensions increasing the sensitivity of the
204 analysis to a range of **SUSY** topologies. Additionally the author has worked extensively
205 in both increasing the statistical precision of electroweak predictions measured from
206 simulation through analytical techniques, and the derivation of a data driven systematic
207 uncertainty through the establishment of closure tests within the control samples of the
208 analysis.

209 Also included within this Chapter is a method to search for **SUSY** signatures which
210 are rich in top and bottom flavoured jet final states. A parametrisation of the b-tagging
211 distribution for different Electroweak processes is used to establish templates, which
212 are then used to estimate the expected number of 3 or 4 b-tagged jet events from **SM**

213 processes. The α_T search is used as a cross check for this template method to establish
214 it's functionality.

215 Finally the interpretation of such results within the framework of a variety of Simplified
216 Model Spectra (**SMS**), which describe an array of possible **SUSY** event topologies is
217 documented in Chapter 5. A description of the statistical model used to derive these
218 interpretations and the possible implications of the results presented in this thesis is
219 discussed within this Chapter. Natural units are used throughout this thesis in which \hbar
220 = c = 1.

Chapter 2.

²²¹ A Theoretical Overview

²²² Within this chapter, a brief introduction and background to the **SM** is given. Its success
²²³ as a rigorously tested and widely accepted theory is discussed as well as the deficiencies
²²⁴ with this theory that hint there this theory is not a complete description of our universe.
²²⁵ The motivations for new physics at the TeV scale and in particular Supersymmetric
²²⁶ theories are outlined within Section (2.3), with the chapter concluding with how an
²²⁷ experimental signature of such theories can be produced and observed at the **LHC**,
²²⁸ Section (2.4).

²²⁹ 2.1. The Standard Model

²³⁰ The **SM** is the name given to the relativistic Quantum Field Theory (**QFT**), where
²³¹ particles are represented as excitations of fields, which describes the interactions and
²³² properties of all the known elementary particles [6][7][8][9]. It is a renormalisable field
²³³ theory which contains three symmetries: $SU(3)$ for colour charge, $SU(2)$ for weak isospin
²³⁴ and $U(1)$ relating to weak hyper charge, which require its Lagrangian \mathcal{L}_{SM} to be invariant
²³⁵ under local gauge transformation.

²³⁶ Within the **SM** theory, matter is composed of spin $\frac{1}{2}$ fermions, which interact with each
²³⁷ other via the exchange of spin-1 gauge bosons. A summary of the known fundamental
²³⁸ fermions and bosons is given in Table 2.1.

²³⁹ Fermions are separated into quarks and leptons of which only quarks interact with
²⁴⁰ the strong nuclear force. Quarks unlike leptons are not seen as free particles in nature,
²⁴¹ but rather exist only within baryons, composed of three quarks with an overall integer

Particle	Symbol	Spin	Charge	Mass (GeV)
First Generation Fermions				
Electron Neutrino	ν_e	$\frac{1}{2}$	0	$< 2.2 \times 10^{-6}$
Electron	e	$\frac{1}{2}$	-1	0.51×10^{-3}
Up Quark	u	$\frac{1}{2}$	$\frac{2}{3}$	$2.3^{+0.7}_{-0.5} \times 10^{-3}$
Down Quark	d	$\frac{1}{2}$	$-\frac{1}{3}$	$4.8^{+0.7}_{-0.3} \times 10^{-3}$
Second Generation Fermions				
Muon Neutrino	ν_μ	$\frac{1}{2}$	0	-
Muon	μ	$\frac{1}{2}$	-1	1.05×10^{-3}
Charm Quark	c	$\frac{1}{2}$	$\frac{2}{3}$	1.275 ± 0.025
Strange Quark	s	$\frac{1}{2}$	$-\frac{1}{3}$	$95 \pm 5 \times 10^{-3}$
Third Generation Fermions				
Tau Neutrino	ν_τ	$\frac{1}{2}$	0	-
Tau	τ	$\frac{1}{2}$	-1	1.77
Top Quark	t	$\frac{1}{2}$	$\frac{2}{3}$	173.5 ± 0.8
Bottom Quark	b	$\frac{1}{2}$	$-\frac{1}{3}$	4.65 ± 0.03
Gauge Bosons				
Photon	γ	1	0	0
W Boson	W^\pm	1	± 1	80.385 ± 0.015
Z Boson	Z	1	0	91.187 ± 0.002
Gluons	g	1	0	0
Higgs Boson	H	0	0	125.3 ± 0.5 [4]

Table 2.1.: The fundamental particles of the SM, with spin, charge and mass displayed. Latest mass measurements taken from [1].

charge, and quark-anti-quark pairs called mesons. Both leptons and quarks are grouped into three generations which have the same properties, but with ascending mass in each subsequent generation.

The gauge bosons mediate the interactions between fermions. The field theories of Quantum Electro-Dynamics (QED) and Quantum Chromo-Dynamics (QCD), yield massless mediator bosons, the photon and eight coloured gluons which are consequences of the gauge invariance of those theories, detailed in Section (2.1.1).

The unification of the electromagnetic and weak-nuclear forces into the current Electroweak theory yield the weak gauge bosons, W^\pm and Z through the mixing of the associated gauge fields. The force carriers of this theory were experimentally detected by

252 the observation of weak neutral current, discovered in 1973 in the Gargamelle bubble
 253 chamber located at European Organization for Nuclear Research (**CERN**) [10], with the
 254 masses of and the weak gauge bosons measured by the UA1 and U2 experiments at the
 255 Super Proton Synchrotron (**SPS**) collider in 1983 [11][12].

256 2.1.1. Gauge Symmetries of the SM

257 Symmetries are of fundamental importance in the description of physical phenomena.
 258 Noether's theorem states that for a dynamical system, the consequence of any symmetry
 259 is an associated conserved quantity [13]. Invariance under translations, rotations, and
 260 Lorentz transformations in physical systems lead to conservation of momentum, energy
 261 and angular momentum.

262 In the **SM**, a quantum theory described by Lagrangian formalism, the weak, strong and
 263 electromagnetic interactions are described in terms of “gauge theories”. A gauge theory
 264 possesses invariance under a set of “local transformations”, which are transformations
 265 whose parameters are space-time dependent. The requirement of gauge invariance within
 266 the **SM** necessitates the introduction of force-mediating gauge bosons and interactions
 267 between fermions and the bosons themselves. Given the nature of the topics covered by
 268 this thesis, the formulation of Electroweak Sector (**EWK**) within the **SM** Lagrangian is
 269 reviewed within this section.

270 The simplest example of the application of the principle of local gauge invariance
 271 within the **SM** is in Quantum Electro-Dynamics (**QED**), the consequences of which
 272 require a massless photon field [14][15].

273 Starting from the free Dirac Lagrangian written as

$$\mathcal{L} = \bar{\psi}(i\gamma^\mu \partial_\mu - m)\psi, \quad (2.1)$$

274 where ψ represents a free non interacting fermionic field, with the matrices $\gamma^\mu, \mu \in$
 275 $0, 1, 2, 3$ defined by the anti commutator relationship $\gamma^\mu \gamma^\nu + \gamma^\nu \gamma^\mu = 2\eta^{\mu\nu} I_4$ where $\eta^{\mu\nu}$ is
 276 the flat space-time metric $(+, -, -, -)$ and I_4 is the 4×4 identity matrix.

277 Under a local U(1) abelian gauge transformation in which ψ transforms as:

$$\psi(x) \rightarrow \psi'(x) = e^{i\theta(x)}\psi(x) \quad \bar{\psi}(x) \rightarrow \bar{\psi}'(x) = e^{i\theta(x)}\bar{\psi}(x) \quad (2.2)$$

278 the kinetic term of the Lagrangian does not remain invariant, due to the partial
279 derivative interposed between the $\bar{\psi}$ and ψ yielding,

$$\partial_\mu \psi \rightarrow e^{i\theta(x)} \partial_\mu \psi + i e^{i\theta(x)} \psi \partial_\mu \theta. \quad (2.3)$$

280 To ensure that \mathcal{L} remains invariant, a modified derivative, D_μ , that transforms
281 covariantly under phase transformations is introduced. In doing this a vector field A_μ
282 with transformation properties that cancel out the unwanted term in (2.3) must also be
283 included,

$$D_\mu \equiv \partial_\mu - ieA_\mu, \quad A_\mu \rightarrow A_\mu + \frac{1}{e} \partial_\mu \theta. \quad (2.4)$$

284 Invariance of the Lagrangian is then achieved by replacing ∂_μ by D_μ :

$$\begin{aligned} \mathcal{L} &= i\bar{\psi}\gamma^\mu D_\mu \psi - m\bar{\psi}\psi \\ &= \bar{\psi}(i\gamma^\mu \partial_\mu - m)\psi + e\bar{\psi}\gamma^\mu \psi A_\mu \end{aligned} \quad (2.5)$$

285 An additional interaction term is now present in the Lagrangian, coupling the Dirac
286 particle to this vector field, which is interpreted as the photon in QED. To regard this
287 new field as the physical photon field, a term corresponding to its kinetic energy must be
288 added to the Lagrangian from Equation (2.5). Since this term must also be invariant
289 under the conditions of Equation (2.4), it is defined in the form $F_{\mu\nu} = \partial^\mu A^\nu - \partial^\nu A^\mu$.

290 This then leads to the Lagrangian of QED:

$$\mathcal{L}_{QED} = \underbrace{i\bar{\psi}\gamma^\mu\partial_\mu\psi - \frac{1}{4}F_{\mu\nu}F^{\mu\nu}}_{\text{kinetic term}} + \underbrace{m\bar{\psi}\psi}_{\text{mass term}} + \underbrace{e\bar{\psi}\gamma^\mu\psi A_\mu}_{\text{interaction term}} \quad (2.6)$$

Within the Lagrangian there remains no mass term of the form $m^2A_\mu A^\mu$, which is prohibited by gauge invariance. This implies that the gauge particle, the photon, must be massless.

2.1.2. The Electroweak Sector and Electroweak Symmetry Breaking

The same application of gauge symmetry and the requirement of local gauge invariance can be used to unify QED and the Weak force in the Electroweak Sector (EWK). The nature of EWK interactions is encompassed within a Lagrangian invariant under transformations of the group $SU(2)_L \times U(1)_Y$.

The weak interactions from experimental observation [16], are known to violate parity and are therefore not symmetric under interchange of left and right helicity fermions. Thus within the SM the left and right handed parts of these fermion fields are treated separately. A fermion field is then split into two left and right handed chiral components, $\psi = \psi_L + \psi_R$, where $\psi_{L/R} = (1 \pm \gamma^5)\psi$.

The $SU(2)_L$ group is the special unitary group of 2×2 matrices U satisfying $UU^\dagger = I$ and $\det(U) = 1$. It may be written in the form $U = e^{-i\omega_i T_i}$, with the generators of the group $T_i = \frac{1}{2}\tau_i$ where τ_i , $i \in 1,2,3$ being the 2×2 Pauli matrices

$$\tau_1 = \begin{pmatrix} 0 & 1 \\ 1 & 0 \end{pmatrix} \quad \tau_2 = \begin{pmatrix} 0 & -i \\ i & 0 \end{pmatrix} \quad \tau_3 = \begin{pmatrix} 1 & 0 \\ 0 & -1 \end{pmatrix}, \quad (2.7)$$

which form a non Abelian group obeying the commutation relation $[T^a, T^b] \equiv if^{abc}T^c \neq 0$. The gauge fields that accompany this group are represented by $\hat{W}_\mu = (\hat{W}_\mu^1, \hat{W}_\mu^2, \hat{W}_\mu^3)$ and act only on the left handed component of the fermion field ψ_L .

³¹¹ One additional generator Y which represents the hypercharge of the particle under
³¹² consideration is introduced through the $U(1)_Y$ group acting on both components of the
³¹³ fermion field, with an associated vector boson field \hat{B}_μ .

³¹⁴ The $SU(2)_L \times U(1)_Y$ transformations of the left and right handed components of ψ
³¹⁵ are summarised by,

$$\begin{aligned}\chi_L &\rightarrow \chi'_L = e^{i\theta(x) \cdot T + i\theta(x)Y} \chi_L, \\ \psi_R &\rightarrow \psi'_R = e^{i\theta(x)Y} \psi_R,\end{aligned}\tag{2.8}$$

³¹⁶ where the left handed fermions form isospin doubles χ_L and the right handed fermions
³¹⁷ are isosinglets ψ_R . For the first generation of leptons and quarks this represents

$$\begin{aligned}\chi_L &= \begin{pmatrix} \nu_e \\ e \end{pmatrix}_L, & \begin{pmatrix} u \\ d \end{pmatrix}_L \\ \psi_R &= e_R, & u_R, d_R\end{aligned}\tag{2.9}$$

³¹⁸ Imposing local gauge invariance within \mathcal{L}_{EWK} is once again achieved by modifying
³¹⁹ the covariant derivative

$$D_\mu = \partial_\mu - \frac{ig}{2} \tau^i W_\mu^i - \frac{ig'}{2} Y B_\mu,\tag{2.10}$$

³²⁰ where g and g' are the coupling constant of the $SU(2)_L$ and $U(1)_Y$ groups respectively.
³²¹ Taking the example of the first generation of fermions defined in Equation.(2.9), with input
³²² hypercharge values of -1 and -2 for χ_L and e_R respectively, would lead to a Lagrangian
³²³ \mathcal{L}_1 of the form,

$$\begin{aligned}\mathcal{L}_1 = &\bar{\chi}_L \gamma^\mu [i\partial_\mu - g \frac{1}{2} \tau \cdot W_\mu - g' (-\frac{1}{2}) B_\mu] \chi_L \\ &+ \bar{e}_R \gamma^\mu [i\partial_\mu - g' (-1) B_\mu] e_R - \frac{1}{4} W_{\mu\nu} \cdot W^{\mu\nu} - \frac{1}{4} B_{\mu\nu} B^{\mu\nu}.\end{aligned}\tag{2.11}$$

324 As in **QED**, these additional gauge fields introduce field strength tensors $B_{\mu\nu}$ and
325 $W_{\mu\nu}$,

$$\hat{B}_{\mu\nu} = \partial_\mu \hat{B}_\nu - \partial_\nu \hat{B}_\mu \quad (2.12)$$

$$\hat{W}_{\mu\nu} = \partial_\mu \hat{W}_\nu - \partial_\nu \hat{W}_\mu - g \hat{W}_\mu \times \hat{W}_\nu \quad (2.13)$$

326 corresponding to the kinetic energy and self coupling of the W_μ fields and the kinetic
327 energy term of the B_μ field.

328 None of these gauge bosons are physical particles, and instead linear combinations of
329 these gauge bosons make up γ and the W and Z bosons, defined as

$$W^\pm = \frac{1}{\sqrt{2}} (W_\mu^1 \mp i W_\mu^2) \quad \begin{pmatrix} Z_\mu \\ A_\mu \end{pmatrix} = \begin{pmatrix} \cos\theta_W & -\sin\theta_W \\ \sin\theta_W & \cos\theta_W \end{pmatrix} \begin{pmatrix} W_\mu^3 \\ B_\mu \end{pmatrix} \quad (2.14)$$

330 where the mixing angle, $\theta_w = \tan^{-1} \frac{g'}{g}$, relates the coupling of the neutral weak and
331 electromagnetic interactions.

332 As in the case of the formulation of the **QED** Lagrangian there remains no mass term
333 for the photon. However this is also the case for the W, Z and fermions in the Lagrangian,
334 contrary to experimental measurement. Any explicit introduction of mass terms would
335 break the symmetry of the Lagrangian and instead mass terms can be introduced through
336 spontaneous breaking of the **EWK** symmetry via the Higgs mechanism.

337 The Higgs mechanism induces spontaneous symmetry breaking through the introduc-
338 tion of a complex scalar SU(2) doublet field ϕ which attains a non-zero Vacuum
339 Expectation Value (**VEV**) [17][18][19][20].

$$\phi = \begin{pmatrix} \phi^+ \\ \phi^0 \end{pmatrix} \quad \text{with} \quad \begin{aligned} \phi^+ &\equiv (\phi_1 + i\phi_2)/\sqrt{2} \\ \phi^0 &\equiv (\phi_3 + i\phi_4)/\sqrt{2} \end{aligned} \quad (2.15)$$

340 The Lagrangian defined in Equation (2.11) attains an additional term \mathcal{L}_{Higgs} of the
341 form

$$\mathcal{L}_{Higgs} = \overbrace{(D_\mu \phi)^\dagger (D^\mu \phi)}^{\text{kinetic}} - \overbrace{\mu^2 \phi^\dagger \phi - \lambda (\phi^\dagger \phi)^2}^{\text{potential } V(\phi)} \quad (\mu^2, \lambda) > 0 \in \mathbb{R},$$

$$\mathcal{L}_{SM} = \mathcal{L}_{EWK} + \mathcal{L}_{Higgs}, \quad (2.16)$$

342 where the covariant derivative D_μ is that defined in Equation (2.10). The last two
343 terms of \mathcal{L}_{Higgs} correspond to the Higgs potential, in which positive real positive values
344 of μ^2 and λ are required to ensure the generation of masses for the bosons and leptons.
345 The minimum of this potential is found at $\phi^\dagger \phi = \frac{1}{2}(\phi_1^2 + \phi_2^2 + \phi_3^2 + \phi_4^2) = \mu^2/\lambda = v^2$,
346 where v represents the **VEV**.

347 Defining the ground state of the ϕ field to be consistent with the $V(\phi)$ minimum, and
348 then expanding around a ground state chosen to maintain an unbroken electromagnetic
349 symmetry thus preserving a zero photon mass [21] leads to

$$\phi_0 = \sqrt{\frac{1}{2}} \begin{pmatrix} 0 \\ v \end{pmatrix}, \quad \phi(x) = e^{i\tau \cdot \theta(x)/v} \sqrt{\frac{1}{2}} \begin{pmatrix} 0 \\ v + h(x) \end{pmatrix}, \quad (2.17)$$

350 where the fluctuations from the vacuum ϕ_0 are parametrized in terms of four real
351 fields, $\theta_1, \theta_2, \theta_3$ and $h(x)$.

352 Choosing to gauge away the three massless Goldstone boson fields by setting $\theta(x)$ to
353 zero and substituting $\phi(x)$ back into kinetic term of \mathcal{L}_{Higgs} from Equation (2.16) leads to
354 mass terms for the W^\pm and Z bosons

$$(D_\mu \phi)^\dagger (D^\mu \phi) = \frac{1}{2}(\partial_\mu h)^2 + \frac{g^2 v^2}{2} W_\mu^+ W^{-\mu} + \frac{v^2 g^2}{8 \cos^2 \theta_w} Z_\mu Z^\mu + 0 A_\mu A^\mu, \quad (2.18)$$

355 where the relations between the physical and electroweak gauge fields from Equation
356 (2.14) are used. The W^\pm and Z bosons can then be determined to be

$$M_W = \frac{1}{2}gv \quad M_Z = \frac{1}{2} \frac{gv}{\cos \theta_w}. \quad (2.19)$$

357 This mechanism is also used to generate fermion masses by introducing a Yukawa
 358 coupling between the fermions and the ϕ field [22], with the coupling strength of a particle
 359 to the ϕ field governing its mass. Additionally a scalar boson h with mass $m_h = v\sqrt{\frac{\lambda}{2}}$, is
 360 also predicted as a result of this spontaneous symmetry breaking and became known as
 361 the Higgs boson. Its discovery by the CMS and ATLAS experiments in 2012 is concrete
 362 evidence to support this method of mass generation within the SM.

363 2.2. Motivation for Physics Beyond the Standard 364 Model

365 As has been described, the SM has proved to be a very successful theory, predicting the
 366 existence of the W^\pm and Z bosons and the top quark long before they were experimentally
 367 observed. However the theory does not accurately describe all observed phenomena and
 368 has some fundamental theoretical flaws that hint at the need for additional extensions to
 369 the current theory.

370 On a theoretical level, the SM is unable to incorporate the gravitational interactions
 371 of fundamental particles within the theory. Whilst at the electroweak energy scales the
 372 relative strength of gravity is negligible compared to the other three fundamental forces,
 373 at much higher energy scales $M_{planck} \sim 10^{18} GeV$ quantum gravitational effects become
 374 increasingly dominant. The failure to reconcile gravity within the SM, demonstrates that
 375 the SM must become invalid at some higher energy scale.

376 Some other deficiencies with the SM include the fact that the predicted rate of
 377 Charge-Parity violation does not account for the matter dominated universe which we
 378 inhabit, and the SM prediction of zero neutrino mass conflicts with the observation of
 379 neutrino flavour mixing, attributed to mixing between neutrino mass eigenstates [23][24].

380 Perhaps one of the most glaring gaps in the predictive power of the SM is that there
 381 exists no candidate to explain the cosmic dark matter observed in galactic structures
 382 through indirect techniques including gravitational lensing and measurement of the
 383 orbital velocity of stars in galactic edges. Any such candidate must be very weakly

³⁸⁴ interacting which must also be stable, owing to the lack of direct detection of the decay
³⁸⁵ products of such an process. Providing a dark matter candidate is of the prime goals
³⁸⁶ which be tackled by any Beyond Standard Model (**BSM**) physics model.

³⁸⁷ The recent discovery of the Higgs boson whilst a significant victory for the predictive
³⁸⁸ power of the **SM**, brings with it still unresolved questions. This issue is commonly
³⁸⁹ described as the “hierarchy problem”.

³⁹⁰ In the absence of new physics between the TeV and Planck scale, calculating beyond
³⁹¹ tree-level contributions to the Higgs mass term given by its self interaction, result in
³⁹² divergent terms that push the Higgs mass up to the planck mass M_{planck} .

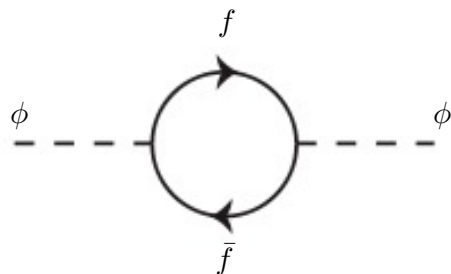


Figure 2.1.: One loop quantum corrections to the Higgs squared mass parameter m_h^2 due to a fermion.

³⁹³ This can be demonstrated by considering the one loop quantum correction to the
³⁹⁴ Higgs mass with a fermion f , shown in Figure 2.1 with mass m_f . The Higgs field couples
³⁹⁵ to f with a term in the Lagrangian $-\lambda_f h \bar{f} f$, yielding a correction of the form [25],

$$\delta m_h^2 = -\frac{|\lambda_f|^2}{8\pi^2} \Lambda^2 + \dots, \quad (2.20)$$

³⁹⁶ where λ_f represents the coupling strength for each type of fermion $\propto m_f$, and Λ the
³⁹⁷ cutoff energy scale at which the **SM** ceases to be a valid theory.

³⁹⁸ To recover the mass of the now discovered Higgs boson would require a fine-tuning of
³⁹⁹ the parameters to cancel out these mass corrections the the Higgs mass to the scale of
⁴⁰⁰ 30 orders of magnitude. This appears as an unnatural solution to physicists and it is
⁴⁰¹ this hierarchy problem that provides one of the strongest motivations for the theory of
⁴⁰² SUperSYmmetry (**SUSY**).

⁴⁰³ 2.3. Supersymmetry Overview

⁴⁰⁴ Supersymmetry provides potential solutions to many of the issues raised in the previous
⁴⁰⁵ section. It provides a dark matter candidate, can explain baryogenesis in the early
⁴⁰⁶ universe and also provides an elegant solution to the hierarchy problem [26][27][28][29].
⁴⁰⁷ At its heart it represents a new space-time symmetry that relates fermions and bosons.
⁴⁰⁸ This symmetry converts bosonic states into fermionic states, and vice versa, see Equation
⁴⁰⁹ (2.21) ,

$$Q|Boson\rangle = |Fermion\rangle \quad Q|Fermion\rangle = |Boson\rangle, \quad (2.21)$$

⁴¹⁰ where the operator Q is the generator of these transformations. Quantum field theories
⁴¹¹ which are invariant under such transformations are called supersymmetric.

⁴¹² This symmetry operator therefore acts upon a particles spin altering it by a half integer
⁴¹³ value. The consequences of the introduction of this additional space-time symmetry
⁴¹⁴ introduce a new rich phenomenology. For example in supersymmetric theories, both
⁴¹⁵ the left handed $SU(2)$ doublet and right handed singlet of fermions will have a spin-0
⁴¹⁶ superpartner, containing the same electric charge, weak isospin, and colour as its **SM**
⁴¹⁷ partner. In the case of the leptons $(\nu_l, l)_L$ will have two superpartners, a sneutrino $\tilde{\nu}_l{}_L$
⁴¹⁸ and a slepton \tilde{l}_L , whilst the singlet l_R also has a superpartner slepton \tilde{l}_R .

⁴¹⁹ Each particle in a supersymmetric theory is paired together with their superpartners
⁴²⁰ as a result of this supersymmetric transformations in a so called supermultiplet. These
⁴²¹ superpartners will then consequently also contribute to the corrections to the Higgs mass.
⁴²² Bosonic and fermionic loops contributing to the correction appear with opposite signs,
⁴²³ and therefore cancellation of these divergent terms will stabilise the Higgs mass, solving
⁴²⁴ the hierarchy problem [30][31].

⁴²⁵ One of the simplest forms of **SUSY** would predict a whole set of supersymmetric
⁴²⁶ partners to their **SM** counterparts with the same mass and interactions. However the
⁴²⁷ currently lack of any experimental evidence for the predicted sparticle spectrum implies
⁴²⁸ **SUSY** must be a broken symmetry in which any sparticle masses must be greater than
⁴²⁹ their SM counterparts.

⁴³⁰ There exist many techniques which can induce supersymmetric breaking [32][33][34].
⁴³¹ Of particular interest to experimental physicists are those at which the breaking scale

⁴³² is of an order that is experimentally accessible to the LHC i.e. \sim TeV scale. Whilst
⁴³³ there is no requirement for supersymmetric breaking to occur at this energy scale, for
⁴³⁴ supersymmetry to provide a solution to the hierarchy problem, it is necessary for this
⁴³⁵ scale to not differ too drastically from the EWK scale [35][36].

⁴³⁶ 2.3.1. R-Parity

⁴³⁷ Some supersymmetric theories also present a solution to the dark matter problem. Such
⁴³⁸ theories can contain a Lightest Supersymmetric Partner (LSP), which matches the criteria
⁴³⁹ of a Weakly Interacting Massive Particle (WIMP) required by cosmological observation
⁴⁴⁰ if R-parity is conserved.

⁴⁴¹ Baryon (B) and Lepton (L) number conservation is forbidden in the SM by renor-
⁴⁴² malisability requirements. The violation of Baryon or Lepton number would result in
⁴⁴³ the proton lifetime much shorter than those set by experimental limits [37]. Another
⁴⁴⁴ symmetry called R-parity is then often introduced to SUSY theories to maintain baryon
⁴⁴⁵ and lepton conservation.

⁴⁴⁶ R-parity is described by the equation

$$R_P = (-1)^{3(B-L)+2s}, \quad (2.22)$$

⁴⁴⁷ where s represents the spin of the particles. $B = \pm \frac{1}{3}$ for quarks/antiquarks and $B = 0$
⁴⁴⁸ for all others, $L = \pm 1$ for leptons/antileptons, $L = 0$ for all others.

⁴⁴⁹ R-parity ensures the stability of the proton in SUSY models, and also has other
⁴⁵⁰ consequences for the production and decay of supersymmetric particles. At particle
⁴⁵¹ colliders supersymmetric particles can only be pair produced, and similarly the decay
⁴⁵² of any produced supersymmetric particle is restricted to a SM particle and a lighter
⁴⁵³ supersymmetric particle as allowed by conservation laws. A further implication of R-
⁴⁵⁴ parity is that once a supersymmetric particle has decayed to the LSP it remains stable,
⁴⁵⁵ unable to decay into a SM particle.

⁴⁵⁶ A LSP would not interact in a detector at a particle collider, leaving behind a missing
⁴⁵⁷ energy \cancel{E}_T signature. The assumption of R-parity and its consequences are used to
⁴⁵⁸ determine the physical motivation and search strategies for SUSY model at the LHC.

459 2.4. Experimental signatures of SUSY at the LHC

460 Should strongly interacting sparticles be within the experimental reach of the LHC, then
461 it is expected that they can be produced in a variety of ways.

- 462 • squark/anti-squark and gluino pairs can be produced via both gluon fusion and
463 quark/anti-quark scattering.
- 464 • a gluino and squark produced together via quark-gluon scattering
- 465 • squark pairs produced via quark-quark scattering

466 Whilst most SUSY searches invoke the requirement of R-parity to explore parameter
467 phase space, there still exist a whole plethora of possible SUSY model topologies which
468 could be discovered at the LHC.

469 During the 2011 run period at a $\sqrt{s} = 7$ TeV particular models were used to benchmark
470 performance and experimental reach of both CMS searches and previous experiments.
471 The Compressed Minimal SuperSymmetric Model (CMSSM) was initially chosen for a
472 number of reasons [38]. One of the most compelling being the reduction from the up to
473 105 new parameters introduced by SUSY in addition to the existing 19 of the SM to that
474 of just 5 free extra free parameters. It was this simplicity, combined with the theory not
475 requiring any fine tuning of particle masses to produce the experimentally verified SM
476 that made it an attractive model to interpret physics results.

477 However recent results from the LHC now strongly disfavour large swathes of CMSSM
478 parameter space [39][40][41]. In the face of such results a more pragmatic model indepen-
479 dent search strategy is now applied across most SUSY searches at the LHC, see Section
480 (2.4.1).

481 As previously stated, a stable LSP that exhibits the properties of a dark matter would
482 be weakly interacting and therefore will not be directly detected in a detector environment.
483 Additionally the cascade decays of supersymmetric particles to the LSP would also result
484 in significant hadronic activity. These signatures can then be characterised through
485 large amounts of hadronic jets (see Section (3.3.1)), leptons and a significant amount of
486 missing energy dependent upon the size of the mass splitting between the LSP and the
487 supersymmetric particle it has decayed from.

488 Whilst the SM contains processes which can exhibit a similar event topology to that
489 described above. The largest contribution of which comes in from the general QCD

490 environment of a hadron collider. A multitude of different analytical techniques are used
491 by experimental physicists to reduce or estimate any reducible or irreducible backgrounds,
492 allowing a possible **SUSY** signature to be extracted. The techniques employed within
493 this thesis are described in great detail within Section (4.1).

494 2.4.1. Simplified Models

495 With such a variety of different ways for a **SUSY** signal to manifest itself, it is necessary
496 to be able to interpret experimental reach through the masses of gluinos and squarks
497 which can excluded by experimental searches rather than on a model specific basis.

498 This is accomplished through **SMS** models, which are defined by a set of hypothetical
499 particles and a sequence of their production and decay [42][43]. In the **SMS** models
500 considered within this thesis, only the production process for the two primary particles
501 are considered. Each primary particle can undergo a direct or a cascade decay through
502 an intermediate new particle. At the end of each decay chain there remains a neutral,
503 undetected **LSP** particle, denoted $\tilde{\chi}_{LSP}$ which can represent a neutralino or gravitino.
504 Essentially it is easier to consider each **SMS** with branching ratios set to 100% The
505 masses of the primary particle and the **LSP** remain as free parameters, in which the
506 absolute value and relative difference between the primary and **LSP** particle alter the
507 kinematics of the event.

508 Different **SMS** models are denoted with a T-prefix, with a summary of the types
509 interpreted within this thesis listed below [44].

- 510 • **T1,T1xxxx**, models represent a simplified version of gluino pair production with
511 each gluino (superpartner to the gluon) undergoing a three-body decay to a quark-
512 antiquark pair and the **LSP** (i.e. $\tilde{g} \rightarrow q\bar{q}\tilde{\chi}_{LSP}$). The resultant final state from this
513 decay is typically 4 jets + \cancel{E}_T in the absence of initial/final state radiation and
514 detector effects. xxxx denotes models in which the quarks are of a specific flavour,
515 typically t or b quark-antiquarks.
- 516 • **T2,T2xx**, models represent a simplified version of squark anti-squark production
517 with each squark undergoing a two-body decay into a light-flavour quark and **LSP**
518 (i.e. $\tilde{q} \rightarrow q\tilde{\chi}_{LSP}$). This results in final states with less jets than gluino mediated
519 production, typically 2 jets + \cancel{E}_T when again ignoring the effect of initial/final state
520 radiation and detector effects. xx models again represent decays in which both the
521 quark and the squark within the decay is of a specific flavour, typically \tilde{t}/t or \tilde{b}/b .

Models rich in b and t quarks are interpreted within this thesis as they remain of particular interest within “Natural SUSY” scenarios [45][46]. The largest contribution to the quadratic divergence in the Higgs mass parameter comes from a loop of top quarks via the Yukawa coupling. Cancellation of these divergences can be achieved in supersymmetric theories by requiring a light right handed top squark, \tilde{t}_R , and left-handed double $SU(2)_L$ doublet containing top and bottom squarks, $(\tilde{\frac{t}{b}})_L$ [47].

These theories therefore solve the hierarchy problem by predicting light \sim EWK scale third generation sleptons, to be accessible at the LHC. Search strategies involving the requirement of b-tagging (see Section (3.3.2)) are used to give sensitivity to these type of SUSY scenarios and are discussed in greater detail within Chapter 5.

Two example decay chains are shown in Figure 2.2; the pair production of gluinos (T1) and the pair production of squarks (T2) decaying into SM particles and LSP’s.

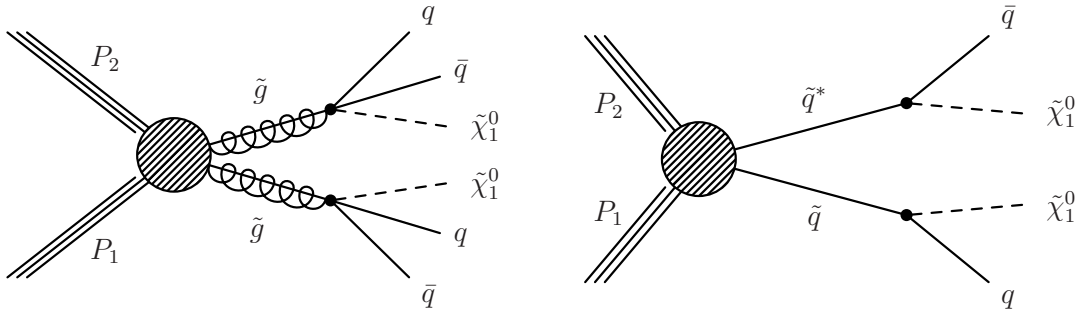


Figure 2.2.: Two example SMS model decays (T1 (left), T2 (right)), which are used in interpretations of physics reach by CMS.

Chapter 3.

⁵³⁴ The LHC and the CMS Detector

⁵³⁵ Probing the SM for signs of new physics would not be possible without the immensely
⁵³⁶ complex electronics and machinery that makes the TeV energy scale accessible for the
⁵³⁷ first time. This chapter will cover the LHC based at European Organization for Nuclear
⁵³⁸ Research (CERN) and the Compact Muon Solenoid (CMS) detector, being the experiment
⁵³⁹ the author is a member of. Section (3.2) serves to introduce an overview of the different
⁵⁴⁰ components of the CMS detector, with more detail spent on those that are relevant in
⁵⁴¹ the search for Supersymmetric particles. Section (3.3) will focus on event and object
⁵⁴² reconstruction again with more emphasis on jet level quantities which are most relevant
⁵⁴³ to the author's analysis research. Finally Section (3.4) will cover work performed by
⁵⁴⁴ the author, as service to the CMS Collaboration, in measuring the performance of the
⁵⁴⁵ Global Calorimeter Trigger (GCT) component of the L1 trigger during the 2012-2013
⁵⁴⁶ run period.

⁵⁴⁷ 3.1. The LHC

⁵⁴⁸ The LHC is a storage ring, accelerator, and collider of circulating beams of protons or
⁵⁴⁹ ions. Housed in the tunnel dug for the Large Electron-Positron collider (LEP), it is
⁵⁵⁰ approximately 27 km in circumference, 100 m underground, and straddles the border
⁵⁵¹ between France and Switzerland outside of Geneva. It is currently the only collider
⁵⁵² in operation that is able to study physics at the TeV scale. A double-ring circular
⁵⁵³ synchrotron, it was designed to collide both proton-proton (pp) and heavy ion (PbPb)
⁵⁵⁴ with a centre of mass energy $\sqrt{s} = 14$ TeV at a final design luminosity of $10^{34}\text{cm}^{-2}\text{s}^{-1}$.

⁵⁵⁵

These counter-circulating beams of protons/Pb ions are merged in four sections around the ring to enable collisions of the beams, with each interaction point being home to one of the four major experiments; A Large Ion Collider Experiment (**ALICE**) [48], A Toroidal LHC ApparatuS (**ATLAS**) [49], Compact Muon Solenoid (**CMS**) [50] and Large Hadron Collider Beauty (**LHC-B**) [51] which record the resultant collisions. The layout of the **LHC** ring is shown in Figure 3.1. The remaining four sections contain acceleration, collimation and beam dump systems. In the eight arc sections, the beams are steered by magnetic fields of up to 8 T provided by super conduction dipole magnets, which are maintained at temperatures of 2 K using superfluid helium. Additional magnets for focusing and corrections are also present in straight sections within the arcs and near the interaction regions where the detectors are situated.

567

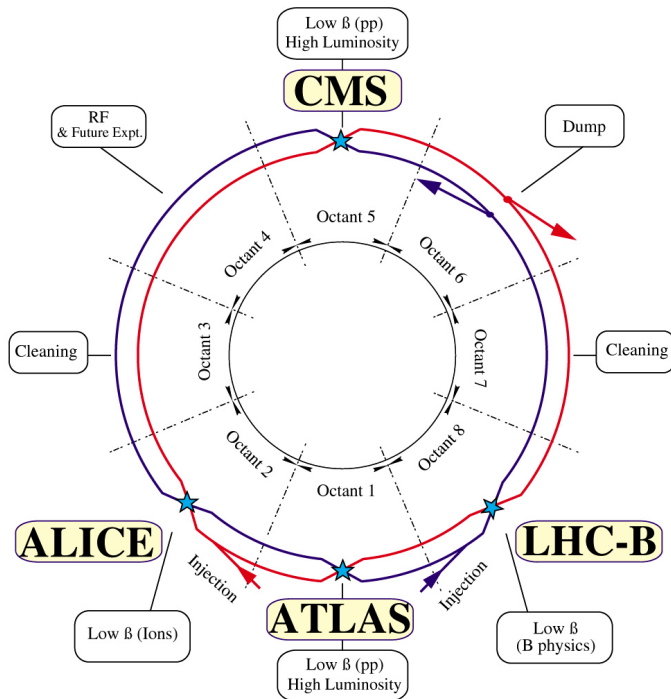


Figure 3.1.: A top down layout of the LHC. [52], with the position of the four main detectors labelled.

Proton beams are formed inside the Proton Synchrotron (**PS**) from bunches of protons 50 ns apart with an energy of 26 GeV. The protons are then accelerated in the Super Proton Synchrotron (**SPS**) to 450 GeV before being injected into the **LHC**. These **LHC** proton beams consists of many “bunches” i.e. approximately 1.1×10^{11} protons localized into less than 1 ns in the direction of motion. Before collision the beams are ramped to 4

573 TeV (2012) per beam in a process involving increasing the current passing through the
 574 dipole magnets. Once the desired \sqrt{s} energy is reached then the beams are allowed to
 575 collide at the interaction points. The luminosity falls regularly as the run progresses as
 576 protons are lost in collisions, and eventually the beam is dumped before repeating the
 577 process again.

578

579 Colliding the beams produced an instantaneous luminosity of approximately $5 \times$
 580 $10^{33} \text{ cm}^{-2}\text{s}^{-1}$ during the 2012 run. The high number of protons in each bunch increases
 581 the likelihood of multiple interactions with each crossing of the counter-circulating
 582 beams. This leads to isotropic energy depositions within the detectors positioned at these
 583 interaction points, increasing the energy scale of the underlying event. This is known as
 584 pile-up and the counteracting of it's effects are important to the many measurements
 585 performed at the LHC.

586 In the early phase of prolonged operation after the initial shutdown the machine
 587 operated in 2010-2011 at 3.5 TeV per beam, $\sqrt{s} = 7 \text{ TeV}$, delivering 6.13 fb^{-1} of data
 588 [53]. During the 2012-2013 run period, data was collected at an increased $\sqrt{s} = 8 \text{ TeV}$
 589 improving the sensitivity of searches for new physics. Over the whole run period 23.3
 590 fb^{-1} of data was delivered of which 21.8 fb^{-1} was recorded by the CMS detector as shown
 591 in Figure 3.2 [53]. A total of 12 fb^{-1} of 8 TeV certified data was collected by October
 592 2012, and it is this data which forms the basis of the results discussed within this thesis.

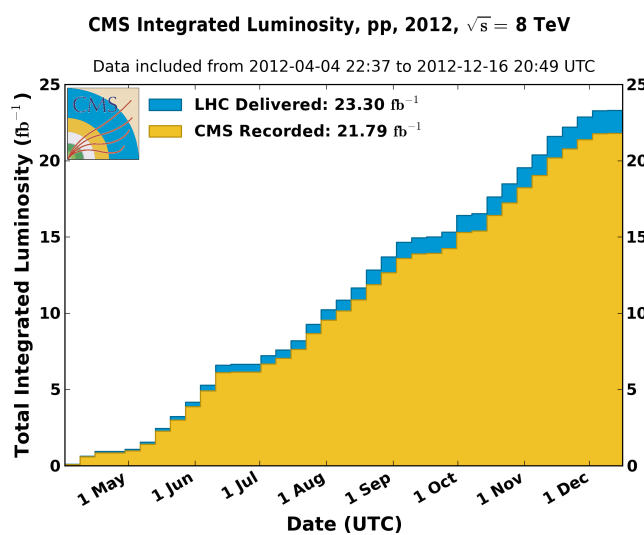


Figure 3.2.: The total integrated luminosity delivered to and collected by CMS during the 2012 8 TeV pp runs.

593 3.2. The CMS detector

594 The Compact Muon Solenoid (**CMS**) detector is one of two general purpose detectors
595 at the **LHC** designed to search for new physics. The detector is designed to provide
596 efficient identification and measurement of many physics objects including photons,
597 electrons, muons, taus, and hadronic showers over wide ranges of transverse momentum
598 and direction. Its nearly 4π coverage in solid angle allows for accurate measurement of
599 global transverse momentum imbalance. These design factors give **CMS** the ability to
600 search for direct production of **SUSY** particles at the TeV scale, making the search for
601 Supersymmetric particles one of the highest priorities among the wide range of physics
602 programmes at **CMS**.

603

604 **CMS** uses a right-handed Cartesian coordinate system with the origin at the interaction
605 point and the z-axis pointing along the beam axis, the x-axis points radially inwards to
606 the centre of the collider ring, with the y-axis points vertically upward. The azimuthal
607 angle, ϕ ranging between $[-\pi, \pi]$ is defined in the x-y plane starting from the x-axis. The
608 polar angle θ is measured from the z axis. The common convention in particle physics is
609 to express an out going particle in terms of ϕ and its pseudorapidity defined as

$$\eta = -\log \tan \left(\frac{\theta}{2} \right). \quad (3.1)$$

610 The variable $\Delta R = \sqrt{\Delta\phi^2 + \Delta\eta^2}$ is commonly used to define angular distance
611 between objects within the detector and additionally energy and momentum is typically
612 measured in the transverse plane perpendicular to the beam line. These values are
613 calculated from the x and y components of the object and are denoted as $E_T = E \sin \theta$
614 and $p_T = \sqrt{p_x^2 + p_y^2}$.

615 3.2.1. Detector Subsystems

616 As the range of particles produced in pp collisions interact in different ways with mat-
617 ter, **CMS** is divided into subdetector systems, which perform complementary roles to
618 identify the identity, mass and momentum of the different physics objects present in
619 each event. These detector sub-systems contained inside **CMS** are wrapped in layers

around a central 13 m long 4 T super conducting solenoid as shown in Figure 3.3. With the endcaps closed , CMS is a cylinder of length 22 m, diameter 15 m, and mass 12.5 kilotons. A more detailed complete description of the detector can be found elsewhere [50].

623

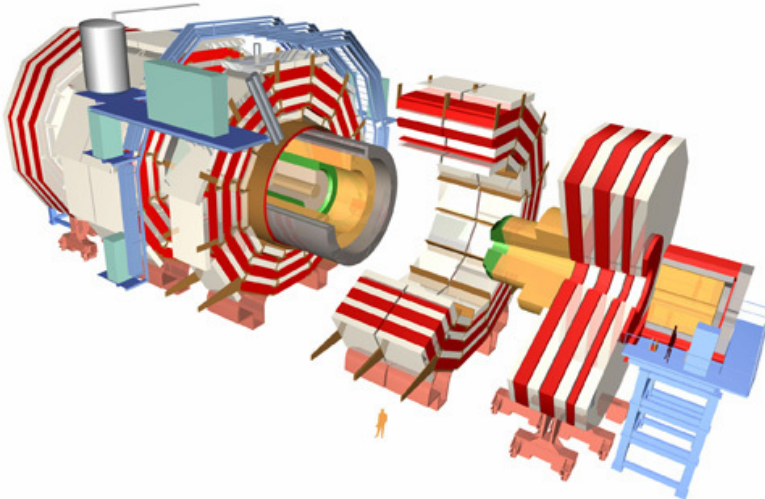


Figure 3.3.: A pictorial depiction of the CMS detector with the main detector subsystems labelled. [54]

624 3.2.2. Tracker

The inner-most subdetector of the barrel is the multi-layer silicon tracker, formed of a pixel detector component encased by layers of silicon strip detectors. The pixel detector consists of three layers of silicon pixel sensors providing measurements of the momentum, position coordinates of the charged particles as they pass, and the location of primary and secondary vertices between 4cm and 10cm transverse to the beam. Outside the pixel detector, ten cylindrical layers of silicon strip detectors extend the tracking system out to a radius of 1.20m from the beam line. The tracking system provides efficient and precise determination of the charges, momenta, and impact parameters of charged particles with the geometry of the tracker extending to cover a rapidity range up to $|\eta| < 2.5$.

634

The tracking system also plays a crucial part in the identification of jets originating from b-quarks through measurement of displaced secondary vertices, which is covered in more detail in Section (3.3.2). The identification of b-jets is important in many searches

638 for natural SUSY models and forms an important part of the inclusive search strategy
639 described within Section (4.2).

640 **3.2.3. Electromagnetic Calorimeter**

641 Immediately outside of the tracker, but still within the magnet core, sits the Electromag-
642 netic CALorimeter (**ECAL**). Covering a pseudorapidity up to $|\eta| < 3$ and comprising
643 of over 75,000 PbWO₄ (lead tungstate) crystals that scintillate as particles deposit energy,
644 the **ECAL** provides high resolution measurements of the electromagnetic showers from
645 photons, electrons in the detector.

646

647 Lead tungstate is used because of its short radiation length ($X_0 \sim 0.9\text{cm}$) and small
648 Molieré radius ($\sim 2.1\text{cm}$) leading to high granularity and resolution. It's fast scintillation
649 time ($\sim 25\text{ns}$) reduces the effects of pile-up due to energy from previous collisions still
650 being read out, and its radiation hardness gives it longevity. The crystals are arranged
651 in modules which surround the beam line in a non-projective geometry, angled at 3°
652 with respect to the interaction point to minimise the risk of particles escaping down the
653 cracks between the crystals.

654

655 The **ECAL** is primarily composed of two sections, the Electromagnetic CALorime-
656 ter Barrel (**EB**) which extends in pseudo-rapidity to $|\eta| < 1.479$ with a crystal front
657 cross section of $22 \times 22 \text{ mm}^2$ and a length of 230 mm corresponding to 25.8 radia-
658 tion lengths, and the Electromagnetic CALorimeter Endcap (**EE**) covering a rapidity
659 range of $1.479 < |\eta| < 3.0$, which consists of two identical detectors on either side of
660 the **EB**. A lead-silicon sampling ‘pre-shower’ detector Electromagnetic CALorimeter
661 pre-Shower (**ES**) is placed before the endcaps to aid in the identification of neutral pions.
662 Their arrangement are shown in Figure 3.4.

663

664 Scintillation photons from the lead tungstate crystals are instrumented with Avalanche
665 Photo-Diodes (**APD**) and Vacuum Photo-Triodes (**VPT**) located in the **EB** and **EE**
666 respectively, converting the scintillating light into an electric signal which is consequently
667 used to determine the amount of energy deposited within the crystal . These instruments
668 are chosen for their resistance under operation to the strong magnetic field of **CMS**. The
669 scintillation of the **ECAL** crystals as well as the response of the **APDs** varies as a function

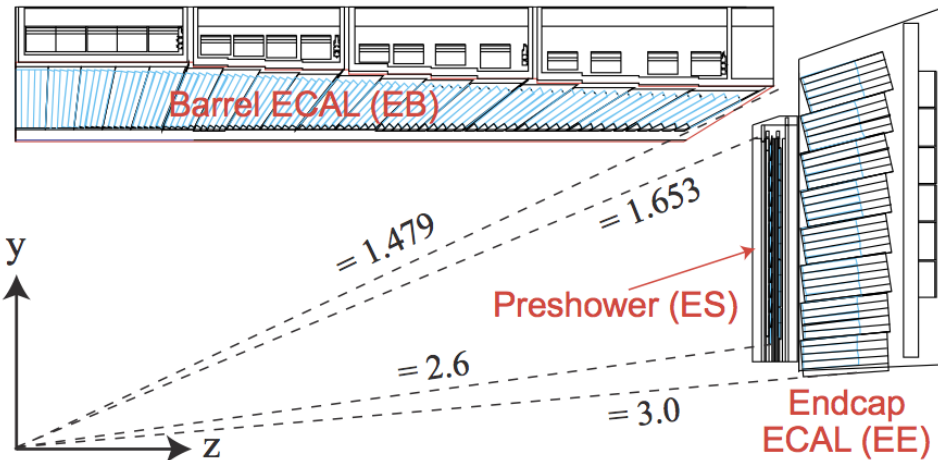


Figure 3.4.: Illustration of the **ECAL** showing the arrangement of the lead tungstate crystals in the **EB** and **EE**. The **ES** is also shown and is located in front of the **EE** [55].

670 of temperature and so cooling systems continually maintain an overall constant **ECAL**
 671 temperature $\pm 0.05^\circ C$.

672 3.2.4. Hadronic Calorimeter

673 Beyond the **ECAL** lies the Hadronic CALorimeter (**HCAL**) which is responsible for
 674 the accurate measurement of hadronic showers, crucial for analyses involving jets or
 675 missing energy signatures. The **HCAL** is a sampling calorimeter which consists of al-
 676 ternating layers of brass absorber and plastic scintillator, except in the hadron forward
 677 ($3.0 < |\eta| < 5.0$) region in which steel absorbers and quartz fibre scintillators are used
 678 because of their increased radiation tolerance. Hadron showers are initiated in the
 679 absorber layers inducing scintillation in the plastic scintillator tiles. These scintillation
 680 photons are converted by wavelength shifting fibres for read-out by hybrid photodiodes.
 681

682 The **HCAL**'s size is constrained to a compact size by the presence of the solenoid,
 683 requiring the placement of an additional outer calorimeter on the outside of the solenoid
 684 to increase the sampling depth of the **HCAL**. A schematic of the **HCAL** can be seen in
 685 Figure 3.5.
 686

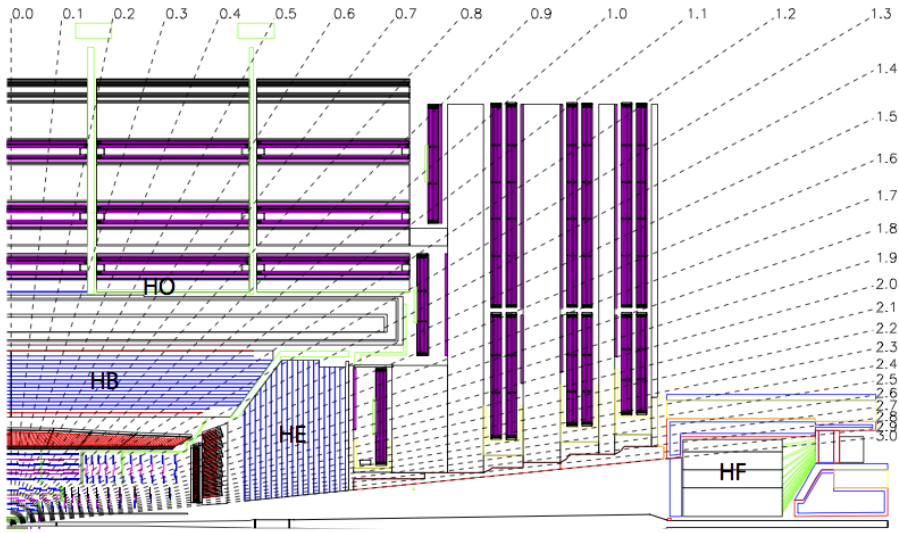


Figure 3.5.: Schematic of the hadron calorimeters in the r-z plane, showing the locations of the **HCAL** components and the **HF**. [50].

The **HCAL** covers the range $|\eta| < 5$ and consists of four subdetectors: the Hadron Barrel (**HB**) $|\eta| < 1.3$, the Hadron Outer (**HO**), the Hadron Endcaps (**HE**) $1.3 < |\eta| < 3.0$ and the Hadron Forward (**HF**). The **HB** is contained between the outer edge of the **ECAL** and the inner edge of the solenoid, formed of 36 azimuthal wedges it is split between two half-barrel segments. The relatively short number of interaction lengths (λ_l , the distance a hadron will travel through the absorber material before it has lost $\frac{1}{e}$ of its energy) within the **HB**, the lowest being $\lambda_l = 5.82$ for $|\eta| = 0$, facilitates the need for the ‘tail catching’ **HO** to increase the sampling depth in the central barrel rapidity region $|\eta| < 1.3$ to 11 interaction lengths . Significant fractions of the hadrons energy will be deposited in the **ECAL** as it passed through the detector. Therefore measurements of hadron energies in the central regions $|\eta| < 3.0$ use both the **ECAL** and **HCAL** to reconstruct the true energy from showering hadrons.

699 3.2.5. Muon Systems

700 Muons being too massive to radiate away energy via Bremsstrahlung, interact little in
701 the calorimeters and mostly pass through the detector until they reach the system of
702 muon detectors which forms the outer most part of the **CMS** detector.

703 Outside of the superconducting solenoid are four muon detection layers interleaved
704 with the iron return yokes which measure the muons energy via ionisation of gas within
705 detector elements. Three types of gaseous chamber are used. The Drift Tube (**DT**),
706 Cathode Stripe Chamber (**CSC**), and Resistive Plate Chamber (**RPC**) systems provide
707 efficient detection of muons with pseudo-rapidity $|\eta| < 2.4$. The best reconstruction
708 performance is obtained when the muon chamber is combined with the inner tracking
709 information to determine muon trajectories and their momenta [56].

710

711 3.3. Event Reconstruction and Object Definition

712 The goal of event reconstruction is to take the raw information recorded by the detector
713 and to compute from it higher-level quantities which can be used at an analysis level.
714 These typically correspond to an individual particle’s energy and momenta, or groups of
715 particles which shower in a narrow cone and the overall global energy and momentum
716 balance of the event. The reconstruction of these objects are described in great detail in
717 [57], however covered below are brief descriptions of those which are most relevant to the
718 analysis detailed in Section (4).

719 3.3.1. Jets

720 Quarks and gluons are produced copiously at the LHC in the hard scattering of partons.
721 As these quarks and gluons fragment, they hadronise and decay into a group of strongly
722 interactive particles and their decay products. These streams of particles travel in the
723 same direction, as they have been “boosted” by the momentum of the primary hadron.
724 These collections of decay products are reconstructed and identified together as a “jet”.

725 At **CMS** jets are reconstructed from energy deposits in the detector using the anti-kt
726 algorithm [58] with size parameter $\Delta R = 0.5$. The anti-kt jet algorithm clusters jets by
727 defining a distance between hard (high p_T) and soft (low p_T) particles such that soft
728 particles are preferentially clustered with hard particles before being clustered between
729 themselves. This produces jets which are robust to soft particle radiation from the pile-up
730 conditions experienced at the **LHC**.

731

732 There are two main type of jet reconstruction used at **CMS**, Calorimeter (Calo) and
733 Particle Flow (PF) jets [59]. Calorimeter jets are reconstructed using both the **ECAL**
734 and **HCAL** cells, combined into calorimeter towers . These calorimeter towers consist of
735 geometrically matched **HCAL** cells and **ECAL** crystals. Electronics noise is suppressed by
736 applying a threshold to the calorimeter cells, with pile-up effects reduced by a requirement
737 placed on the tower energy [60]. Calorimter jets are the jets used within the analyses
738 described in this thesis.

739 PF jets are formed from combining information from all of the **CMS** subdetectors
740 systems to determine which final state particles are present in the event. Generally,
741 any particle is expected to produce some combination of a track in the silicon tracker,
742 a deposit in the calorimeters, or a track in the muon system. The PF jet momentum
743 and spatial resolutions are greatly improved with respect to calorimeter jets, as the use
744 of the tracking detectors and of the high granularity of **ECAL** allows resolution and
745 measurement of charged hadrons and photons inside a jet, which together constitute \sim
746 85% of the jet energy [61].

747 The jets reconstructed by the clustering algorithm in **CMS** typically have an energy
748 that differs to the ‘true’ energy measured by a perfect detector. This stems from the
749 non-linear and nonuniform response of the calorimeters as well as other residual effects
750 including pile-up and underlying events, and therefore additional corrections are applied
751 to recover a uniform relative response as a function of pseudo-rapidity. These are applied
752 as separate sub corrections [62].

- 753 • A PU correction is first applied to the jet. It subtracts the average extra energy
754 deposited in the jet that comes from other vertices present in the event and is
755 therefore not part of the hard jet itself.
- 756 • p_T and η dependant corrections derived from Monte Carlo simulations are used to
757 account for the non-uniform response of the detector.
- 758 • p_T and η residual corrections are applied to data only to correct for difference
759 between data and Monte Carlo. The residual is derived from QCD dijet samples
760 and the p_T residual from $\gamma+$ jet and $Z+$ jets samples in data.

761 **3.3.2. B-tagging**

762 The decays of b quarks are suppressed by small CKM matrix elements. As a result, the
763 lifetimes of b-flavoured hadrons, produced in the fragmentation of b quarks, are relatively
764 long; \mathcal{O} 1ps. The identification of jets origination from b quarks is very important for
765 searches for new physics and for measurements of standard model processes.

766

767 Many different algorithms developed by CMS select b-quark jets based on variables
768 such as the impact parameters of the charged-particle tracks, the properties of recon-
769 structed decay vertices, and the presence or absence of a lepton, or combinations thereof
770 [63]. One of the most efficient of which is the Combined Secondary Vertex (CSV) which
771 operates based on secondary vertex and track-based lifetime information, benchmarked
772 in ‘Loose’, ‘Medium’ and ‘Tight’ working points, of which the medium point is the tagger
773 used within the α_T search detailed in Section (4.1).

774 Using the CSV tagger, a likelihood-based discriminator distinguishes between jets
775 from b-quarks, and those from charm or light quarks and gluons, which is shown in Figure
776 3.6. The minimum thresholds on the discriminator for each working point correspond to
777 the misidentification probability for light-parton jets of 10%, 1%, and 0.1%, respectively,
778 in jets with an average p_T of about 80 GeV.

779 The b-tagging performance is evaluated to measure the b-jet tagging efficiency ϵ_b ,
780 and the misidentification probability of charm ϵ_c and light-parton jets ϵ_s . The tagging
781 efficiencies for each of these three jet flavours are compared between data and MC
782 simulation, from which a series of p_T and $|\eta|$ binned jet corrections are determined,

$$SF_{b,c,s} = \frac{\epsilon_{b,c,s}^{data}}{\epsilon_{b,c,s}^{MC}}. \quad (3.2)$$

783 These are collectively named ‘Btag Scale Factors’ and allow MC simulation to accu-
784 rately reflect the running conditions and performance of the tagging algorithm in data.
785 Understanding of the b-tagging efficiency is essential in order to minimise systematic
786 uncertainties in physics analyses that employ b-tagging.

787

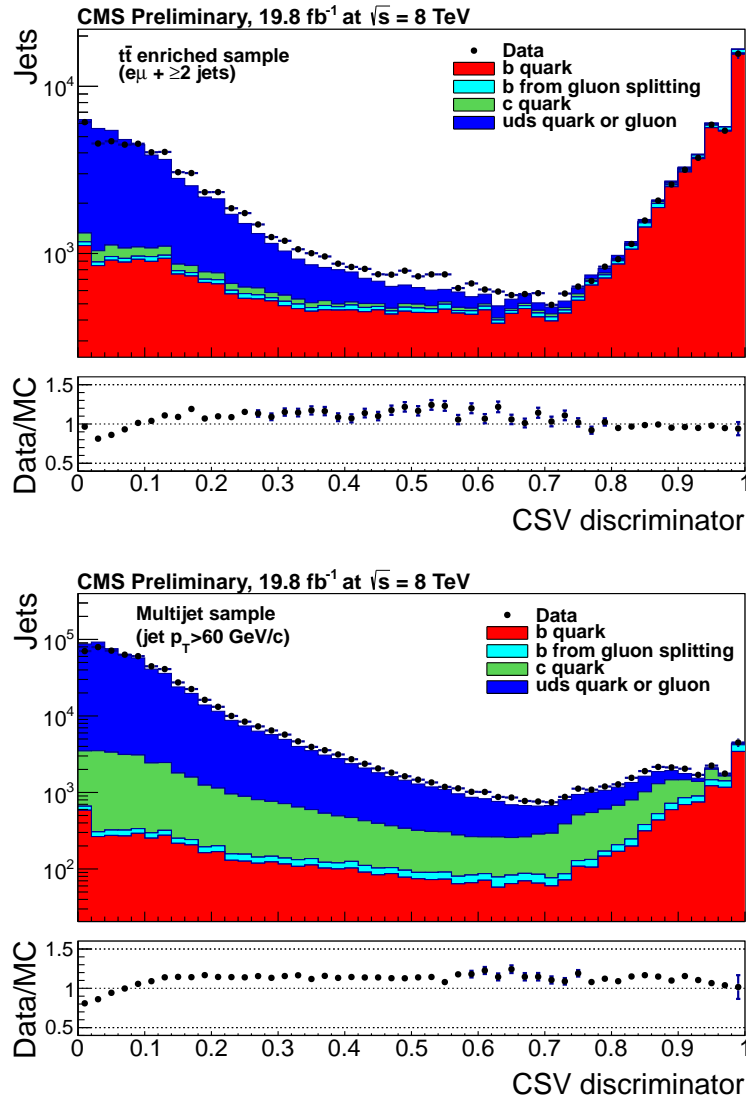


Figure 3.6.: CSV algorithm discriminator values in enriched $t\bar{t}$ (top) and inclusive multi jet samples (bottom) for b,c and light flavoured jets [64]. Working points are determined from the misidentification probability for light-parton jets to be tagged as a b-jet and are given as 0.244, 0.679 and 0.898 for L,M and T working points respectively.

788 The b-tagging efficiency is measured in data using several methods applied to multi
 789 jet events, primarily based on a sample of jets enriched in heavy flavour content. One
 790 method requires the collection of events with a soft muon within a cone $\Delta R < 0.4$ around
 791 the jet axis. Because the semileptonic branching fraction of b hadrons is significantly
 792 larger than that for other hadrons, these jets are more likely to arise from b quarks than
 793 from another flavour, with the resultant momentum component of the muon transverse
 794 to the jet axis larger for muons from b-hadron decays than from light or charm jets.

Additionally the performance of the tagger can also be benchmarked in $t\bar{t}$ events where in the SM, the top quark is expected to decay to a W boson and a b quark about 99.8% of the time [1]. Further selection criteria is applied to these events to further enrich the b quark content of these events. The methods to identify b-jets in data are discussed in great detail at [65]. The jet flavours are determined in simulation using truth level information and are compared to data to determine the correction scale factors (SF_b), which are displayed for the CSVM tagger in Figure 3.7.

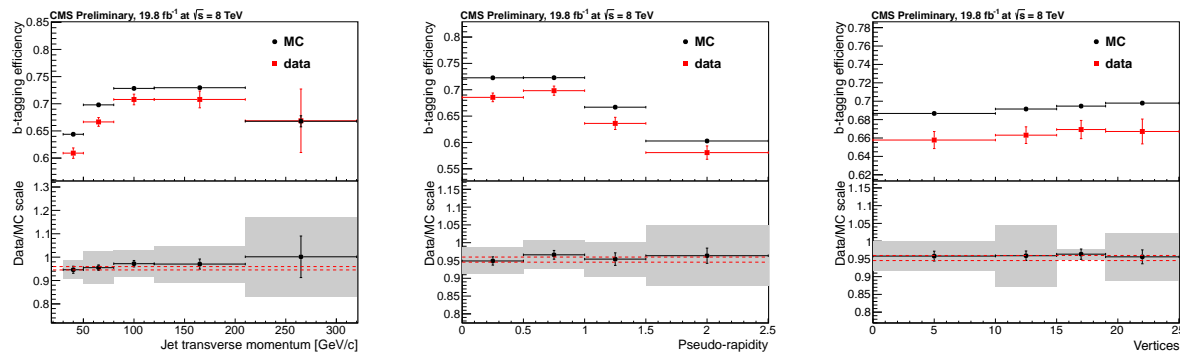


Figure 3.7.: Measured in $t\bar{t} \rightarrow$ di-lepton events using the CSVM tagger: (upper panels) b-tagging efficiencies and (lower panels) data/MC scale factor SF_b as a function of (left) jet p_T , (middle) jet $|\eta|$ and (right) number of primary vertices. In the lower panels, the grey filled areas represent the total statistical and systematic uncertainties, whereas the dotted lines are the average SF_b values within statistical uncertainties.

The measurement of the misidentification probability for light-parton jets relies on the inversion of tagging algorithms, selecting non-b jets using the same variables and techniques used in benchmarking the b-tagging efficiency. The scale factors (SF_s) to be applied to MC are shown in Figure 3.8 for the CSVM tagger.

3.4. Triggering System

With bunch crossings separated by just 25 ns, the rate at which data from all collisions would have to be written out and processed would be unfeasible. A two-tiered triggering system is applied at CMS in order to cope with the high collision rate of protons. The CMS trigger is designed to use limited information from each event to determine whether to record the event, reducing the rate of data taking to manageable levels whilst ensuring a high efficiency of interesting physics object events are selected.

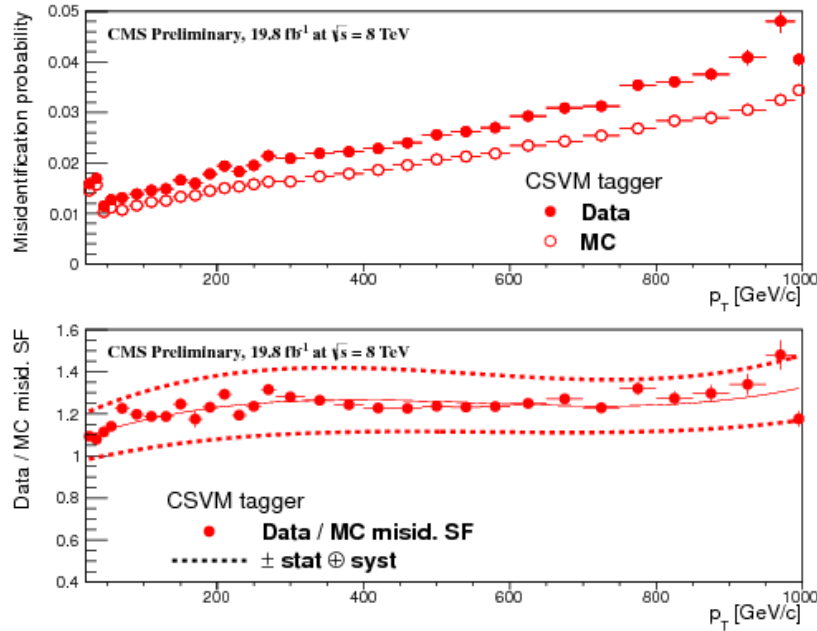


Figure 3.8.: For the **CSVM** tagging criterion: (top) misidentification probability in data (filled circles) and simulation (open circles); (bottom) scale factor for the misidentification probability. The last p_T bin in each plot includes all jets with $p_T > 1000$ GeV. The solid curve is the result of a polynomial fit to the data points. The dashed curves represent the overall statistical and systematic uncertainties on the measurements.

813 The **L1** is a pipelined, dead-timeless system based on custom-built electronics [66],
 814 and is a combination of several sub systems which is shown pictorially in Figure 3.9. The
 815 L1 system is covered in more detail within the following section along with a description
 816 of the service work undertaken by the author to benchmark the performance of the L1
 817 calorimeter trigger during the 2012 8 TeV run period.

818 The Higher Level Trigger (**HLT**) is a large farm of commercial computers [67]. The
 819 **HLT** processes events with software reconstruction algorithms that are more detailed,
 820 giving performance more similar to the reconstruction used offline. The **HLT** reduces
 821 the event rate written to disk by a factor of ~ 500 (~ 200 Hz). The recorded events are
 822 transferred from **CMS** to the **CERN** computing centre, where event reconstruction is
 823 performed, and then distributed to **CMS** computing sites around the globe for storage
 824 and analysis.

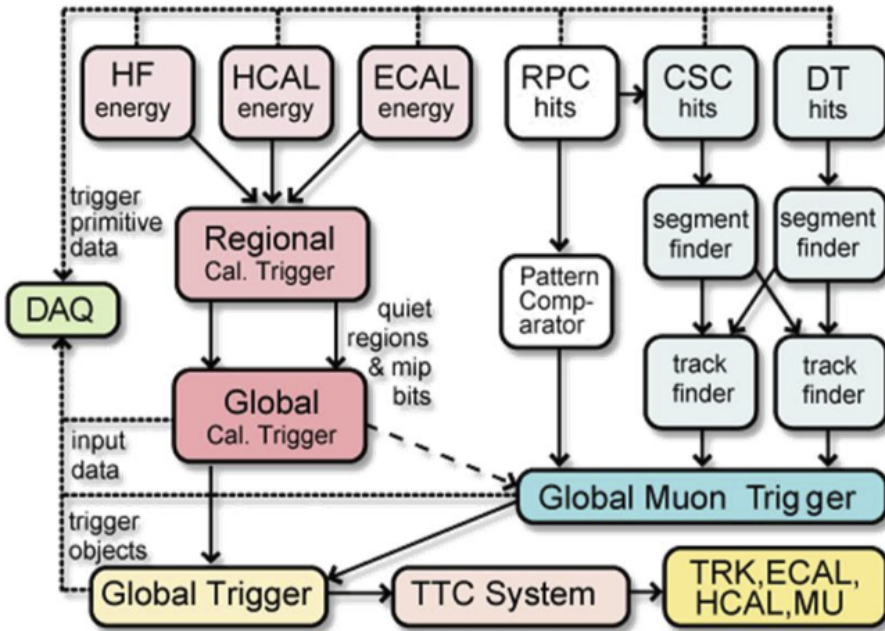


Figure 3.9.: The CMS L1 Trigger system.

3.4.1. The Level-1 Trigger

The L1 trigger reduces the rate of events collected from 40 MHz to ~ 100 kHz using information from the calorimeters and muon chambers, but not the tracker. A tree system of triggers is used to decide whether to pass on an event to the HLT for further reconstruction. Firstly the calorimeter and muon event information is kept separate, with local reconstruction of objects ($\mu, e, \gamma, \text{jets}$) performed by the Regional Calorimeter Trigger (RCT) and Regional Muon Trigger (RMT) respectively. The RCT generates up to 72 isolated and non-isolated electromagnetic objects. These are sorted by rank, which is equivalent to transverse energy E_T , with the four highest ranked electromagnetic objects being passed via the Global Calorimeter Trigger (GCT) and Global MuonTrigger (GMT) to the Global Trigger (GT).

In the L1 GCT, coarse measurements of the energy deposited in the electromagnetic and hadronic calorimeters are combined and by using sophisticated algorithms the following physics objects are formed:

- isolated and non-isolated electromagnetic objects (e and γ);
- hadronic jets in the central and forward sections of the hadronic calorimeters;

- hadronically decaying tau leptons;
- total transverse energy (E_T), the scalar sum of the energy measured at L1, and missing transverse energy (\cancel{E}_T), defined as the vector sum of the energy of L1 objects;
- total transverse jet energy (H_T), the scalar sum of the energy of all L1 jet objects, and missing transverse jet energy (\cancel{H}_T), defined as the vector sum of the energy of L1 jets, are calculated from uncorrected L1 jets.

In addition quantities suitable for triggering minimum bias events, forward physics and beam background events are calculated. Additionally relevant muon isolation information is also passed on to the **GMT** for decisions involving the muon triggers where it is combined with information from across the three muon sub-systems. The resultant final accept/reject decision at **L1** is then performed by the **GT** based on the objects received from the **GCT** and **GMT** (e/γ , μ , jets, E_T , \cancel{E}_T , H_T).

The L1 trigger is therefore of upmost importance to the functioning of the detector. Without a high-performing trigger and a good understanding of its performance, there would be no data to analyse. Observations of how the L1 trigger performance is affected by changing **LHC** running conditions over the 2012 run period and also the introduction of a jet seed threshold to the L1 jet trigger algorithm is presented in the following Sections (3.4.2 - 3.4.6).

3.4.2. L1 Trigger Jet Algorithm

The L1 jet trigger uses the transverse energy sums computed in the calorimeter (both hadronic and electromagnetic) trigger regions. Each region consists of 4×4 trigger tower windows, spanning a region of $\Delta\eta \times \Delta\phi = 0.087 \times 0.087$ in pseudorapidity-azimuth. The jet trigger uses a 3×3 calorimeter region (112 trigger towers) sliding window technique which spans the full (η, ϕ) coverage of the **CMS** calorimeter as shown in Figure 3.10.

In forming a L1 jet is it required that the central region to be higher than the eight neighbouring regions $E_{T\text{central}} > E_{T\text{surround}}$. Additionally a minimum threshold of 5 GeV on $E_{T\text{central}}$ was introduced during the 2012 run period to suppress noise from pile-up, the effects of which are shown in Section (3.4.4).

The L1 jets are characterised by the E_T , summed over the 3×3 calorimeter regions, which corresponds to 12×12 trigger towers in barrel and endcap or 3×3 larger **HF**

872 towers in the **HF**. The ϕ size of the jet window is the same everywhere, whilst the η
873 binning gets somewhat larger at high η due to calorimeter and trigger tower segmentation.
874 The jets are labelled by (η, ϕ) indexes of the central calorimeter region.

875 Jets with $|\eta| > 3.0$ are classified as forward jets, whereas those with $|\eta| < 3.0$ are
876 classified as central. The four highest energy central, forward and τ jets in the calorimeter
877 are passed through Look Up Table (**LUT**)'s, which apply a programmable η -dependent
878 jet energy scale correction. These are then used to make L1 trigger decisions.

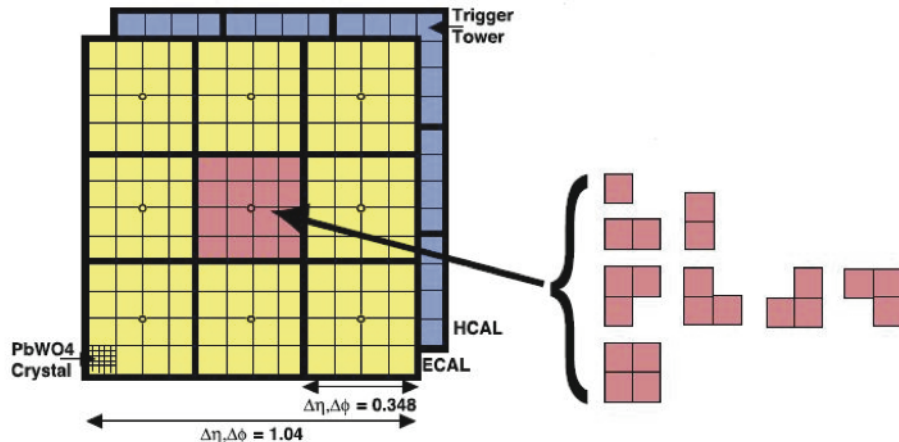


Figure 3.10.: Illustration of the Level-1 jet finding algorithm.

879 The performance of the L1 jets is evaluated with respect to offline jets, which are
880 taken from the standard Calo jet and the PF jet reconstruction algorithms of **CMS**.
881 Jets are corrected for pile-up and detector effects as described in [3.3.1](#). A moderate
882 level of noise rejection is applied to the offline jets by selecting jets passing the “loose
883 identification criteria for both Calo and PF. These criteria are summarised in Appendix
884 ([A.1](#)).

885 3.4.3. Measuring L1 Jet Trigger Efficiencies

886 The L1 jet efficiency is defined as the fraction of leading offline jets which were matched
887 with a L1 tau or central jet above a certain trigger threshold, divided by all the leading
888 offline jets in the event. This quantity is then plotted as a function of the offline jet E_T ,
889 η and ϕ .

890 The efficiency is determined by matching the L1 and reconstructed offline jets spatially
891 in $\eta - \phi$ space. This is done by calculating the minimum separation in ΔR between the

892 highest offline reconstructed jet in E_T ($E_T > 10$ GeV, $|\eta| < 3$) and any L1 jet. A jet will
 893 be matched if this value is found to be < 0.5 . Should more than one jet satisfy this, the
 894 jet closest in ΔR is taken as the matched jet. The matching efficiency is close to 100%,
 895 above ? 30(45) GeV for run 2012B(C) data (see Appendix (??)).

896 Each efficiency curve is fitted with a function which is the cumulative distribution
 897 function of an Exponentially Modified Gaussian (EMG) distribution:

$$898 f(x; \mu, \sigma, \lambda) = \frac{\lambda}{2} \cdot e^{\frac{\lambda}{2}(2\mu + \lambda\sigma^2 - 2x)} \cdot \text{erfc}\left(\frac{\mu + \lambda\sigma^2 - x}{\sqrt{2}\sigma}\right) \quad (3.3)$$

where erfc is the complementary error function defined as:

$$\text{erfc}(x) = 1 - \text{erf}(x) = \frac{2}{\sqrt{\pi}} \int_x^\infty e^{-t^2} dt.$$

899 In this functional form, the parameter μ determines the point of 50% of the plateau
 900 efficiency and the σ gives the resolution. This parametrisation is used to benchmark
 901 the efficiency at the plateau, the turn-on points and resolution for each L1 Jet trigger.
 902 The choice of function is purely empirical. Previous studies used the error function
 903 alone, which described the data well at high threshold values but could not describe the
 904 efficiencies well at lower thresholds [68].

905 The efficiency turn-on curves for various L1 jet thresholds are evaluated as a function
 906 of the offline reconstructed jet E_T for central jets with $|\eta| < 3$. These are measured using
 907 single isolated μ triggers which have high statistics, and are orthogonal and therefore
 908 unbiased to the hadronic triggers under study. The efficiency is calculated with respect to
 909 offline Calo and PF Jets in Figure 3.11. Table 3.1 shows the values of these parameters,
 910 calculated for three example L1 single jet triggers taken from 2012 8 TeV data.

911 The results from the L1 single jet triggers shows good performance for both Calo and
 912 PF jets. A better resolution for Calo jets with respect to L1 jets quantities is observed.
 913 This effect is due to Calo jet reconstruction using the same detector systems as in L1 jets,
 914 whereas with PF jet construction using tracker and muon information, a more smeared
 915 resolution when compared to L1 is expected.

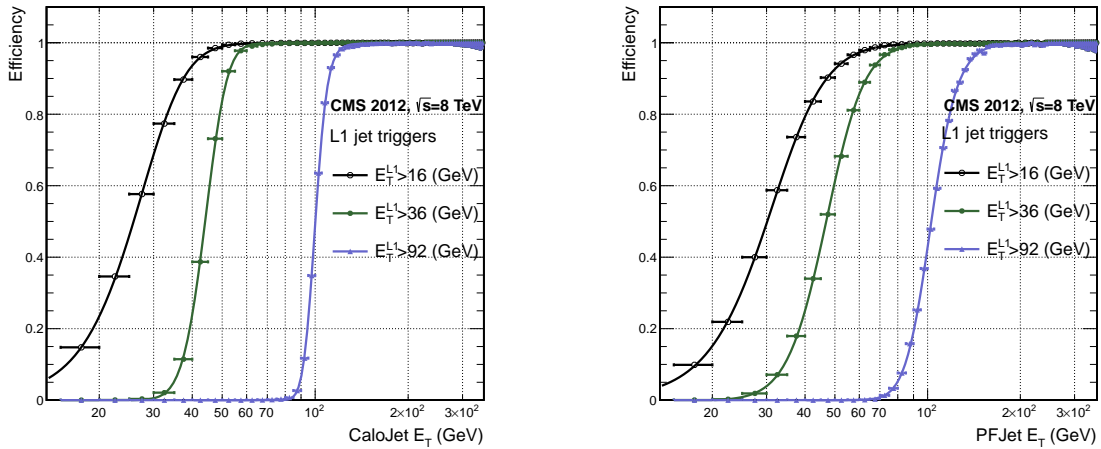


Figure 3.11.: L1 jet efficiency turn-on curves as a function of the offline CaloJet E_T (left) and PFJet E_T (right), measured in 2012 Run Period C data and collected with an isolated single μ data sample.

Trigger	Calo		PF	
	μ	σ	μ	σ
L1_SingleJet16	21.09 ± 0.03	7.01 ± 0.02	22.17 ± 0.04	7.83 ± 0.03
L1_SingleJet36	41.15 ± 0.05	5.11 ± 0.02	39.16 ± 0.06	8.04 ± 0.03
L1_SingleJet92	95.36 ± 0.13	5.62 ± 0.03	90.85 ± 0.19	11.30 ± 0.10

Table 3.1.: Results of a cumulative EMG function fit to the turn-on curves for L1 single jet triggers in run 2012 Run Period C, measured in an isolated μ data sample. The turn-on point, μ , and resolution, σ , of the L1 jet triggers are measured with respect to offline Calo Jets (left) and PF Jets (right).

3.4.4. Effects of the L1 Jet Seed

Between run period B and C of the 2012 data taking period, a jet seed threshold was introduced into the L1 trigger jet algorithm. There was previously no direct requirement made on the energy deposited in the central region. The introduction of a jet seed threshold required that the central region have $E_T \geq 5$ GeV, and was introduced to counteract the effects of high pile up running conditions which create a large number of soft non-collimated jets, that are then added to the jets from the primary interaction or other soft jets from other secondary interactions [69]. This in turn causes a large increase in trigger rate due to the increase in the likelihood that the event causes the L1 trigger to fire. This was implemented to maintain trigger thresholds by cutting the rate of events recorded without significant reduction in the efficiency of physics events of interest.

The effect of the introduction of this jet seed threshold between these two run periods is benchmarked through a comparison of the efficiency of the L1 jet triggers with respect to offline Calo jets shown in Figure 3.12, and the L1 H_T trigger efficiency in Figure 3.14 which is compared to offline H_T constructed from Calo jets with $E_T \geq 40\text{GeV}$.

To negate any effects from different pile-up conditions in the run periods, the efficiencies are measured in events which contain between 15 and 20 primary vertices as defined in Appendix (A.2).

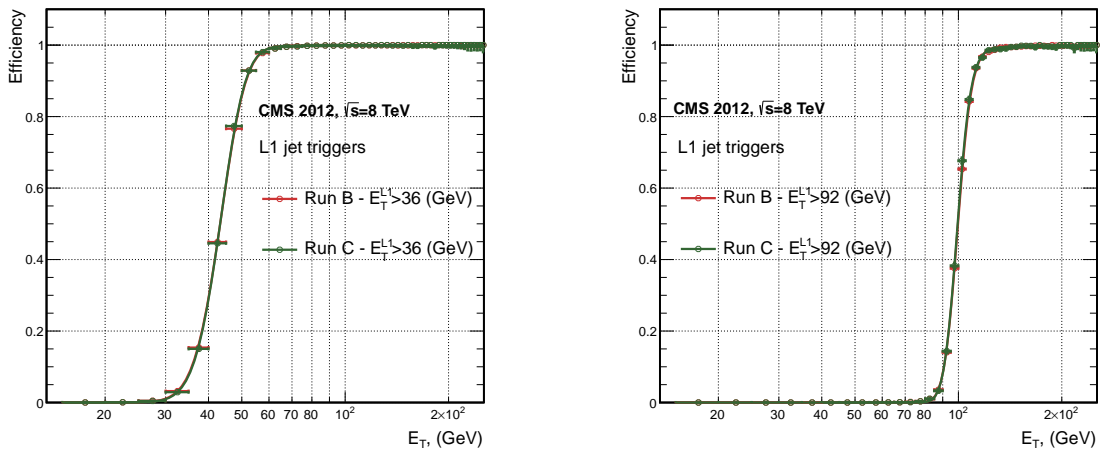


Figure 3.12.: L1 jet efficiency turn-on curves as a function of the offline CaloJet E_T , measured for the L1 SingleJet 36 and 92 trigger in 2012 run period B and C collected with an isolated single μ' sample.

It can be seen that the performance of the $E_T > 36, 92$ single jet are almost identical, with the jet seed having no measurable effect on these triggers as shown in Table 3.2 .

Trigger	2012B		2012C	
	μ	σ	μ	σ
L1_SingleJet36	40.29 ± 0.04	5.34 ± 0.02	40.29 ± 0.11	5.21 ± 0.05
L1_SingleJet92	94.99 ± 0.09	5.93 ± 0.06	94.82 ± 0.29	5.74 ± 0.18

Table 3.2.: Results of a cumulative EMG function fit to the turn-on curves for L1 single jet triggers in the 2012 run period B and C, preselected on an isolated muon trigger. The turn-on point μ and resolution σ of the L1 jet triggers are measured with respect to offline Calo Jets in run B (left) and run C (right).

For the H_T triggers, a large increase in rate during high pile-up conditions is expected. This is due to the low energy threshold required for a jet to be added to the L1 H_T sum,

which is compiled from all uncorrected L1 jets formed in the RCT. The introduction of the jet seed threshold removes the creation of many of these soft low E_T jets, thus lowering the H_T calculation at L1. The effect on the trigger cross section for L1 H_T 150 trigger can be seen in Figure 3.13.

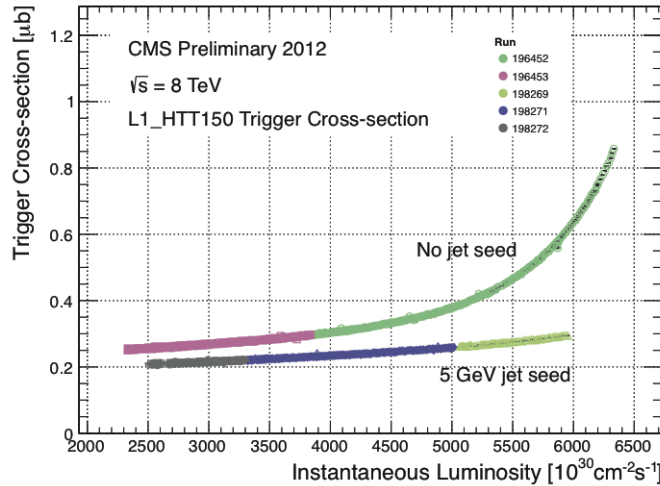


Figure 3.13.: Trigger cross section for the L1HTT150 trigger path. Showing that a 5 GeV jet seed threshold dramatically reduces the dependance of cross section on the instantaneous luminosity for L1 H_T triggers [70].

Different behaviours for the trigger turn ons between these run periods are therefore expected. The turn on point is observed to shift to higher H_T values after the introduction of the jet seed threshold, whilst having a sharper resolution due to less pile-up jets being included the H_T sum, the results are shown in Table 3.3.

Trigger	2012B		2012C	
	μ	σ	μ	σ
L1 HT-100	157.5 ± 0.08	32.9 ± 0.08	169.8 ± 0.08	28.7 ± 0.03
L1 H1-150	230.9 ± 0.02	37.3 ± 0.01	246.4 ± 0.16	31.8 ± 0.05

Table 3.3.: Results of a cumulative EMG function fit to the turn-on curves for H_T in run 2012 B and C, preselected on an isolated single μ trigger. The turn-on point μ , resolution σ of the L1 H_T triggers are measured with respect to offline H_T formed from CaloJets with a $E_T \geq 40$ in run period B (left) and C (right).

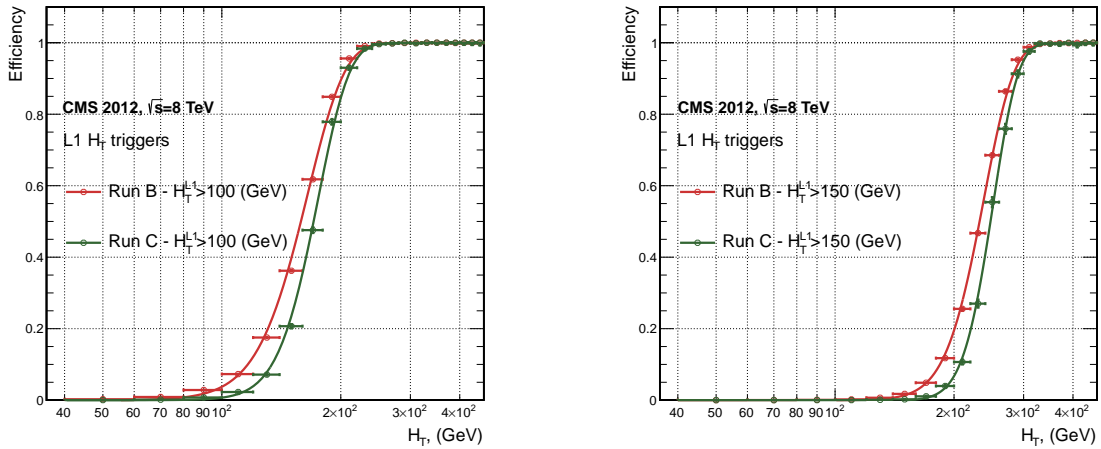


Figure 3.14.: L1 H_T efficiency turn-on curves as a function of the offline CaloJet H_T , measured for the L1 H_T 100 and 150 trigger during the run 2012 B and C collected using an isolated single μ triggered sample.

946 3.4.5. Robustness of L1 Jet Performance against Pile-up

947 The performance of the L1 single jet triggers is evaluated in different pile-up conditions
 948 to benchmark any dependence on pile-up. Three different pile-up bins of 0-10, 10-20 and
 949 >20 vertices are defined, reflecting the low, medium and high pile-up running conditions
 950 at CMS in 2012. This is benchmarked relative to Calo and PF jets for the run 2012 C
 951 period where the jet seed threshold is applied, with L1 single jet thresholds of 16, 36 and
 952 92 GeV, shown in Figure 3.15. The results of fits to these efficiency turn-on curves are
 953 given in Table 3.4 and Table 3.5 for Calo and PF jets respectively.

Vertices	0-10		11-20		> 20	
	μ	σ	μ	σ	μ	σ
L1_SingleJet16	19.9 ± 0.1	6.1 ± 0.3	20.8 ± 0.1	6.5 ± 0.1	22.3 ± 0.2	7.5 ± 0.1
L1_SingleJet36	41.8 ± 0.1	4.6 ± 0.1	40.9 ± 0.1	5.1 ± 0.1	40.6 ± 0.6	5.9 ± 0.2
L1_SingleJet92	95.9 ± 0.2	5.4 ± 0.1	95.2 ± 0.2	5.6 ± 0.1	94.5 ± 0.6	6.2 ± 0.3

Table 3.4.: Results of a cumulative EMG function fit to the efficiency turn-on curves for L1 single jet triggers in the 2012 run period C, measured from isolated μ triggered data. The turn-on point, μ , and resolution, σ , of the L1 jet triggers are measured with respect to offline Calo jets in low (left), medium (middle) and high (right) pile-up conditions.

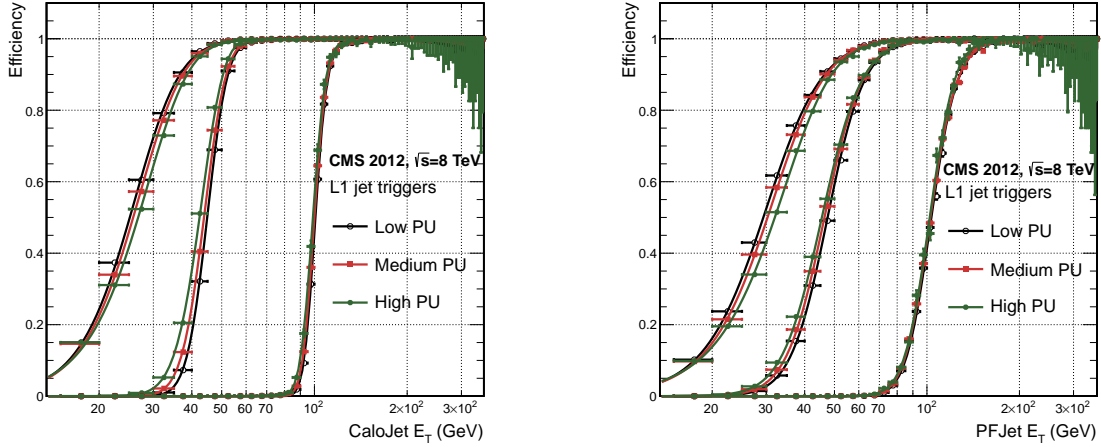


Figure 3.15.: L1 jet efficiency turn-on curves as a function of the leading offline E_T Calo (left) and PF (right) jet, for low, medium and high pile-up conditions.

Vertices	0-10		11-20		> 20	
	μ	σ	μ	σ	μ	σ
L1_SingleJet16	21.1 ± 0.1	7.16 ± 0.05	22.34 ± 0.1	7.9 ± 0.1	24.6 ± 0.2	9.5 ± 0.1
L1_SingleJet36	39.6 ± 0.1	7.4 ± 0.1	38.4 ± 0.1	7.4 ± 0.1	37.1 ± 0.2	7.5 ± 0.1
L1_SingleJet92	91.6 ± 0.3	11.3 ± 0.2	90.4 ± 0.3	11.2 ± 0.1	92.0 ± 0.9	12.1 ± 0.4

Table 3.5.: Results of a cumulative EMG function fit to the efficiency turn-on curves for Level-1 single jet triggers in the 2012 run period C, measured from isolated μ triggered data. The turn-on point, μ , and resolution, σ , of the L1 jet triggers are measured with respect to offline PF jets in low (left), medium (middle) and high (right) pile-up conditions.

954 No significant drop in efficiency is observed in the presence of a high number of
 955 primary vertices. The increase in hadronic activity in higher pile-up conditions, combined
 956 with the absence of pile-up subtraction for L1 jets, results in the expected observation of
 957 a decrease in the μ value of the efficiency turn-ons as a function of pile-up, while the
 958 resolution, σ of the turn-ons are found to gradually worsen as expected with increasing
 959 pile-up.

960 These features are further emphasised when shown as a function of

$$\frac{(L1 E_T - \text{Offline } E_T)}{\text{Offline } E_T} \quad (3.4)$$

in bins of matched leading offline jet E_T , of which the individual fits can be found in Appendix (B.2). Each of these distributions are fitted with an EMG function as defined in Equation (3.3).

The μ , σ and λ values extracted for the low, medium and high pile-up conditions are shown for Calo and PF jets in Figure 3.16 and Figure 3.17 respectively. The central value of $\frac{(L1 E_T - \text{Offline } E_T)}{\text{Offline } E_T}$ is observed to increases as a function of jet E_T , whilst the resolution is also observed to improve at higher offline jet E_T .

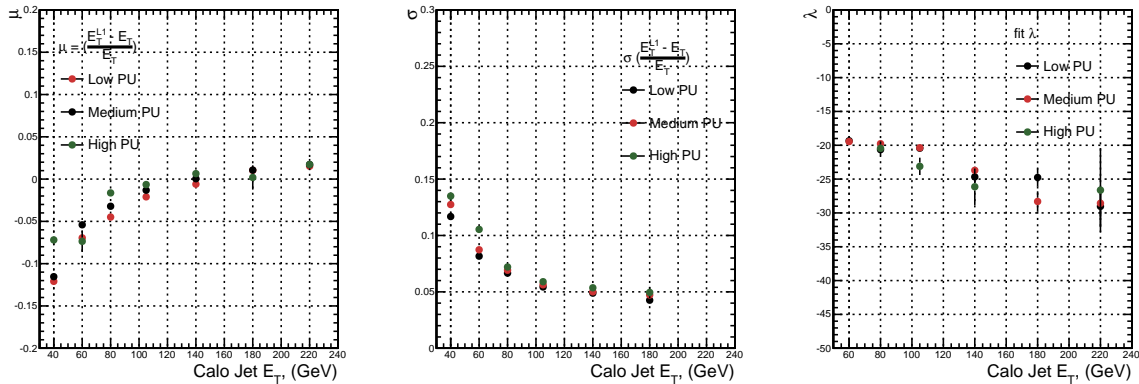


Figure 3.16.: Fit values from an EMG function fitted to the resolution plots of leading Calo jet E_T measured as a function of $\frac{(L1 E_T - \text{Offline } E_T)}{\text{Offline } E_T}$ for low, medium and high pile-up conditions. The plots show the mean μ (left), resolution σ (middle) of the Gaussian as well as the decay term λ (right) of the exponential.

The resolution of other L1 energy sum quantities, H_T , \not{E}_T and $\sum E_T$ parameterised as in Equation (3.4), can be found in Appendix (B.3). The same behaviour observed for the single jet triggers is also found for these quantities, where in the presence of higher pile-up the μ values are shifted to higher values, with a worsening resolution, σ again due to the increase in soft pile-up jets and the absence of pile-up subtraction at L1.

3.4.6. Summary

The performance of the CMS Level-1 Trigger has been studied and evaluated for jets and energy sum quantities using data collected during the 2012 LHC 8TeV run. These studies include the effect of introduction of a 5 GeV jet seed threshold into the jet algorithm configuration, the purpose of which is to mitigate the effects of pile-up on the rate of L1 triggers whilst not adversely affecting the efficiency of these triggers. No significant

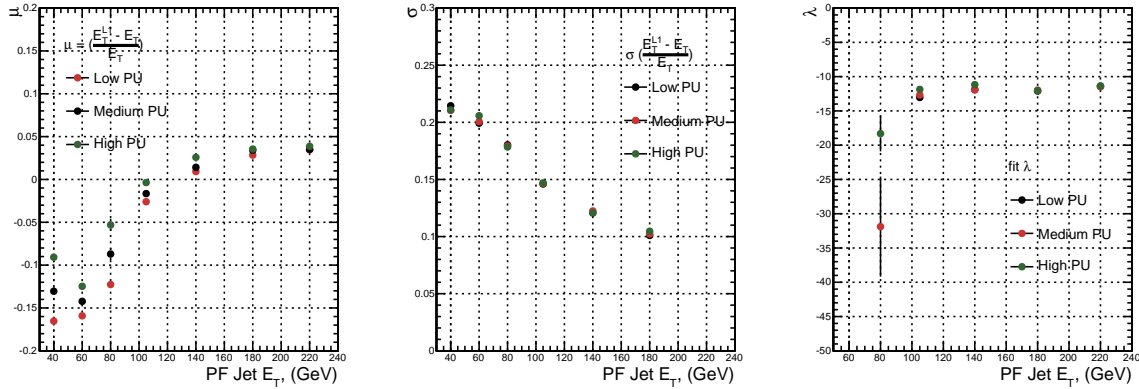


Figure 3.17.: Fit values from an **EMG** function fitted to the resolution plots of leading PF jet E_T measured as a function of $\frac{(L1\ E_T - Offline\ E_T)}{Offline\ E_T}$ for low and medium pile-up conditions. The plots show the mean μ (left), resolution σ (middle) of the Gaussian as well as the decay term λ (right) of the exponential.

979 change in performance is observed with this change and good performance is observed
 980 for a range of L1 quantities.

Chapter 4.

981 SUSY searches in Hadronic Final 982 States

983 In this chapter a model independent search for **SUSY** in hadronic final states with \cancel{E}_T
984 using the α_T variable and b-quark multiplicity is introduced and described in detail. The
985 results presented are based on a data sample of pp collisions collected in 2012 at $\sqrt{s} = 8$
986 TeV, corresponding to an integrate luminosity of $11.7 \pm 0.5 \text{ fb}^{-1}$.

987 The kinematic variable α_T is motivated as a variable to provide strong rejections
988 of QCD backgrounds, whilst maintaining sensitivity to possible a **SUSY** signal within
989 Section (4.1). The search and trigger strategy in addition to the event reconstruction
990 and selection are outlined within Sections (4.2-4.4).

991 The method in which the **SM** background is estimated using an analytical technique
992 to improve statistical precision at higher b-tag multiplicities is detailed within Section
993 (4.5), with a discussion on the impact of b-tagging and mis-tagging scale factors between
994 data and MC on any background predictions. Finally a description of the formulation of
995 appropriate systematic uncertainties applied to the background predictions to account for
996 theoretical uncertainties and limitations in the simulation modelling of event kinematics
997 and instrumental effects is covered in Section (4.6).

998 In addition to the α_T search, a complimentary technique is discussed as a means to
999 predict the distribution of 3 and 4 reconstructed b-quark jets in an event in Section
1000 (4.7). The recent discovery of the Higgs boson has made third-generation “Natural **SUSY**”
1001 models attractive, given that light top and bottom squarks are a candidate to stabilise
1002 divergent loop corrections to the Higgs boson mass.

1003 Using the α_T search as a base, a simple templated fit is employed to estimate the
1004 **SM** background in higher b-tag multiplicities (3-4) from a region of a low number
1005 of reconstructed b-jets (0-2). The predictions using this technique are first tested in
1006 simulation before being compared to the **SM** background predictions obtained from the
1007 α_T search.

1008 The experimental reach of the analysis discussed within this thesis is interpreted in
1009 two classes of **SMS** models, the topologies of which are detailed in Section (2.4.1). The
1010 **SMS** models considered in this analysis are summaries in Table 4.1. For each model, the
1011 **LSP** is assumed to be the lightest neutralino.

1012 Within Table 4.1 is also defined reference points, parameterised in terms of parent
1013 gluino/squark and **LSP** sparticle masses, m_{parent} and m_{LSP} , respectively, which are used
1014 within the following two chapters to demonstrate potential yields within the signal region
1015 of the search. The masses are chosen to reflect parameter space which is within the
1016 expect sensitivity reach of the search.

Model	Production/decay mode	Reference model	
		m_{parent}	m_{LSP}
G1 (T1)	$pp \rightarrow \tilde{g}\tilde{g}^* \rightarrow q\bar{q}\tilde{\chi}_1^0 q\bar{q}\tilde{\chi}_1^0$	700	300
G2 (T1bb)	$pp \rightarrow \tilde{g}\tilde{g}^* \rightarrow b\bar{b}\tilde{\chi}_1^0 b\bar{b}\tilde{\chi}_1^0$	900	500
G3 (T1tt)	$pp \rightarrow \tilde{g}\tilde{g}^* \rightarrow t\bar{t}\tilde{\chi}_1^0 t\bar{t}\tilde{\chi}_1^0$	850	250
D1 (T2)	$pp \rightarrow \tilde{q}\tilde{q}^* \rightarrow q\tilde{\chi}_1^0 \bar{q}\tilde{\chi}_1^0$	600	250
D2 (T2bb)	$pp \rightarrow \tilde{b}\tilde{b}^* \rightarrow b\tilde{\chi}_1^0 \bar{b}\tilde{\chi}_1^0$	500	150
D3 (T2tt)	$pp \rightarrow \tilde{t}\tilde{t}^* \rightarrow t\tilde{\chi}_1^0 \bar{t}\tilde{\chi}_1^0$	400	0

Table 4.1.: A summary of the **SMS** models interpreted in this analysis, involving both direct (D) and gluino-induced (G) production of squarks and their decays. Reference models are also defined in terms of parent and **LSP** sparticle mass

1017 4.1. An introduction to the α_T search

1018 The experimental signature of **SUSY** signal in the hadronic channel would manifest as a
1019 final state containing energetic jets and \cancel{E}_T . The search focuses on topologies where new
1020 heavy supersymmetric, R-parity conserving particles are pair-produced in pp collisions.
1021 These particles decaying to a **LSP** escape the detector undetected, leading to significant
1022 missing energy and missing hadronic transverse energy,

$$\mathcal{H}_T = \left| \sum_{i=1}^n p_T^{jet_i} \right|, \quad (4.1)$$

1023 defined as the vector sum of the transverse energies of jets selected in an event.
1024 Energetic jets produced in the decay of these supersymmetric particles also can produce
1025 significant visible transverse energy,

$$H_T = \sum_{i=1}^n E_T^{jet_i}, \quad (4.2)$$

1026 defined as the scalar sum of the transverse energies of jets selected in an event.

1027 A search within this channel is greatly complicated in a hadron collider environment,
1028 where the overwhelming background comes from inherently balanced multi-jet (“QCD”)
1029 events which are produced with an extremely large cross section as demonstrated within
1030 Figure 4.1. \cancel{E}_T can appear in such events with a substantial mis-measurement of jet
1031 energy or missed objects due to detector miscalibration or noise effects.

1032 Additional **SM** background from **EWK** processes with genuine \cancel{E}_T from escaping
1033 neutrinos comprise the irreducible background within this search and come mainly from:

- 1034 • $Z \rightarrow \nu\bar{\nu}$ + jets,
- 1035 • $W \rightarrow l\nu$ + jets in which a lepton falls outside of detector acceptance, or the lepton
1036 decays hadronically $\tau \rightarrow \text{had}$,
- 1037 • $t\bar{t}$ with at least one leptonic W decay,
- 1038 • small background contributions from DY, single top and Diboson (WW,ZZ,WZ)
1039 processes.

1040 The search is designed to have a strong separation between events with genuine and
1041 “fake” \cancel{E}_T which is achieved primarily through the dimensionless kinematic variable, α_T
1042 [71][72].

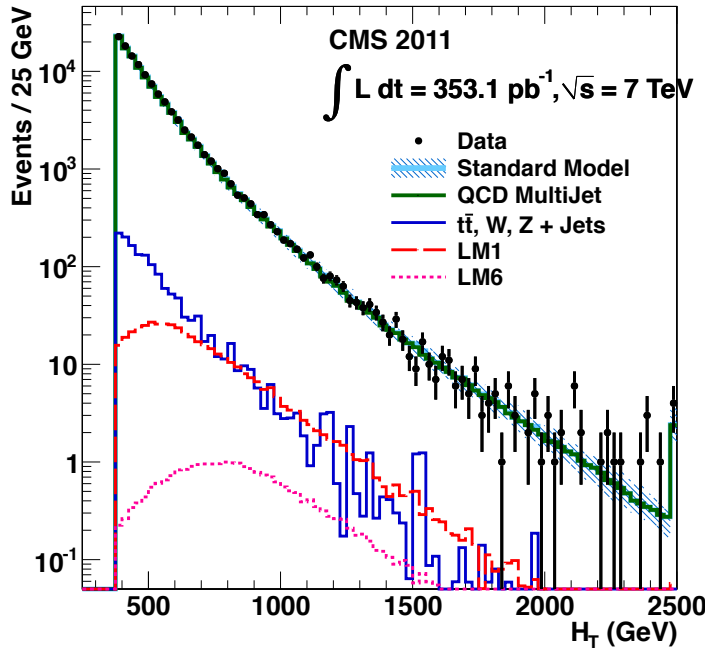


Figure 4.1.: Reconstructed offline H_T for 11.7fb^{-1} of data after a basic pre-selection. Sample is collected from prescaled H_T triggers. Overlaid are expectations from MC simulation of EWK processes as well as a reference signal model (labelled D2 from Table 4.1).

1043 4.1.1. The α_T variable

1044 For a perfectly measured di-jet QCD event, conservation laws dictate that they must be
 1045 produced back-to-back and of equal magnitude. However in di-jet events with real \cancel{E}_T , both of these jets are produced independently of one another, depicted in Figure 4.2.

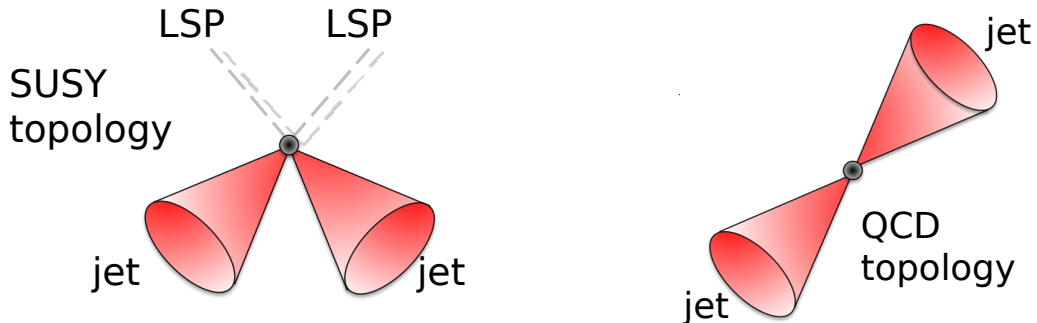


Figure 4.2.: The event topologies of background QCD dijet events (right) and a generic SUSY signature with genuine \cancel{E}_T (left).

1047 Exploiting this feature leads to the formulation of α_T in di-jet systems defined as,

$$\alpha_T = \frac{E_T^{j2}}{M_T}, \quad (4.3)$$

1048 where E_T^{j2} is the transverse energy of the least energetic of the two jets and M_T
1049 defined as:

$$M_T = \sqrt{\left(\sum_{i=1}^2 E_T^{j_i}\right)^2 - \left(\sum_{i=1}^2 p_x^{j_i}\right)^2 - \left(\sum_{i=1}^2 p_y^{j_i}\right)^2} \equiv \sqrt{H_T^2 - \cancel{H}_T^2}. \quad (4.4)$$

1050 A perfectly balanced di-jet event i.e. $E_T^{j_1} = E_T^{j_2}$ would give an $\alpha_T = 0.5$, where as
1051 events with jets which are not back-to-back, for example in events in which a W or Z
1052 recoils off a system of jets, α_T can achieve values in excess of 0.5.

1053 α_T can be extended to apply to any arbitrary number of jets, undertaken by modelling
1054 a system of n jets as a di-jet system, through the formation of two pseudo-jets [73].
1055 The two pseudo-jets are built by merging the jets present in the event such that the 2
1056 pseudo-jets are chosen to be as balanced as possible, i.e the $\Delta H_T \equiv |E_T^{pj_1} - E_T^{pj_2}|$ is
1057 minimised between the two pseudo jets. Using Equation (4.4), α_T can be rewritten as,

$$\alpha_T = \frac{1}{2} \frac{H_T - \Delta H_T}{\sqrt{H_T^2 - \cancel{H}_T^2}} = \frac{1}{2} \frac{1 - \Delta H_T/H_T}{\sqrt{1 - (\cancel{H}_T/H_T)^2}}. \quad (4.5)$$

1058 The distribution of α_T for the two jet categories used within this analysis, 2,3 and
1059 ≥ 4 jets, is shown in the Figure 4.3, demonstrating the ability of the α_T variable to
1060 discriminate between multi jet events and EWK processes with genuine \cancel{E}_T in the final
1061 state.

1062 The α_T requirement used within the search is chosen to be $\alpha_T > 0.55$ to ensure
1063 that the QCD multijet background is negligible even in the presence of moderate jet
1064 mis-measurement. There still remains other effects which can cause multijet events to
1065 artificially have a large α_T value, which are discussed in detail in Section (4.4).

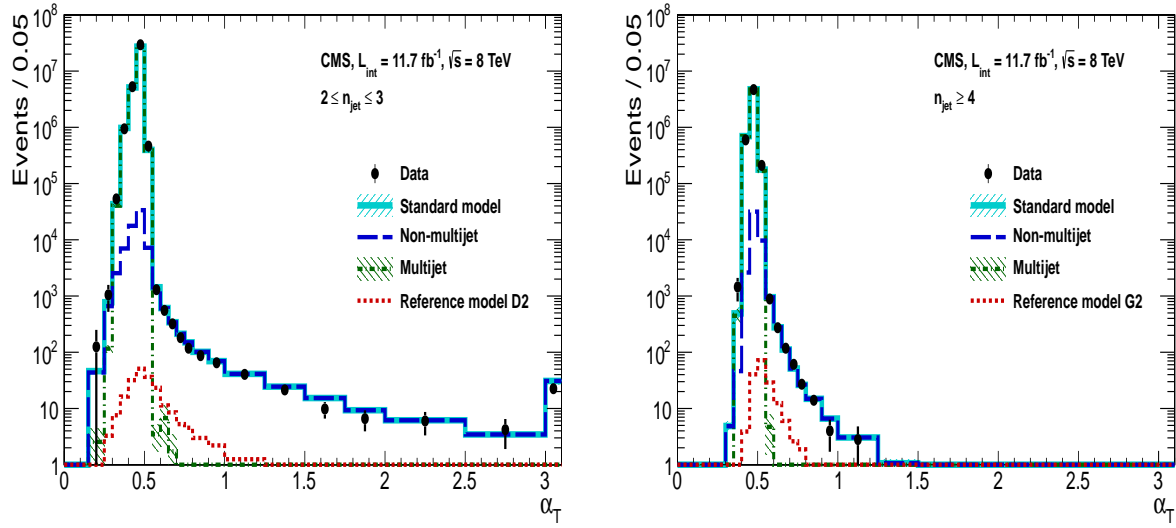


Figure 4.3.: The α_T distributions for the low 2-3 (left) and high ≥ 4 (right) jet multiplicities after a full analysis selection and shown for $H_T > 375$. Data is collected using both prescaled H_T triggers and dedicated α_T triggers for below and above $\alpha_T = 0.55$ respectively. . Expected yields as given by simulation are also shown for multijet events (green dash-dotted line), EWK backgrounds with genuine \cancel{E}_T (blue long-dashed line), the sum of all SM processes (cyan solid line) and the reference signal model D2 (left, red dotted line) or G2 (right, red dotted line).

1066 4.2. Search Strategy

1067 The aim of the analysis presented in this thesis is to identify an excess of events in data
 1068 over the SM background expectation in multi-jet final states and significant \cancel{E}_T . The
 1069 essential suppression of the dominant QCD background for such a search is addressed by
 1070 the α_T variable described in the previous section. For estimation of the remaining EWK
 1071 backgrounds, three independent data control samples are used to predict the different
 1072 processes that compose the background :

- 1073 • $\mu + \text{jets}$ to determine $W + \text{jets}$, $t\bar{t}$ and single top backgrounds,
- 1074 • $\gamma + \text{jets}$ to determine the irreducible $Z \rightarrow \nu\bar{\nu} + \text{jets}$ background,
- 1075 • $\mu\mu + \text{jets}$ to determine the irreducible $Z \rightarrow \nu\bar{\nu} + \text{jets}$ background.

1076 These control samples are chosen to both be rich in specific EWK processes, be free of
 1077 QCD multi-jet events and to also be kinematically similar to the hadronic signal region
 1078 that they are estimating the backgrounds of, see Section (4.2.1).

1079 To remain inclusive to a large range of possible **SUSY** models, the signal region is
1080 binned in the following categories to allow for increased sensitivity in the interpretation
1081 of results for different **SUSY** topologies:

1082 **Sensitivity to a range of SUSY mass splittings**

1083 The hadronic signal region is defined by $H_T > 275$, divided into eight bins in H_T .

- 1084 – Two bins of width 50 GeV in the range $275 < H_T < 375$ GeV,
1085 – five bins of width 100 GeV in the range $375 < H_T < 875$ GeV,
1086 – and a final open bin, $H_T > 875$ GeV.

1087 The choice at low H_T is driven primarily by trigger constraints. The mass difference
1088 between the **LSP** and the particle that it decays from is an important factor in the
1089 amount of hadronic activity in the event.

1090 A large mass splitting will lead to hard high p_T jets which contribute to the H_T
1091 sum. From Figure 4.1 it can be seen that the **SM** background falls sharply at high
1092 H_T values, therefore a large number of H_T bins will lead to easier identification
1093 of such signals. Conversely smaller mass splittings lead to softer jet p_T 's which will
1094 subsequently fall into the lower H_T range.

1095 **Sensitivity to production method of SUSY particles**

1096 The production mechanism of any potential **SUSY** signal can lead to different event
1097 topologies. One such way to discriminate between gluino ($g\tilde{g}$ - “high multiplicity”),
1098 and direct squark ($q\tilde{q}$ - “low multiplicity”) induced production of **SUSY** particles is
1099 realised through the number of reconstructed jets in the final state.

1100 The analysis is thus split into two jet categories : 2-3 jets , ≥ 4 jets to give sensitivity
1101 to both of these mechanisms.

1102 **Sensitivity to “Natural SUSY” via tagging jets from b-quarks**

1103 Jets originating from bottom quarks (b-jets) are identified through vertices that
1104 are displaced with respect to the primary interaction. The algorithm used to tag
1105 b-jets is the Combined Secondary Vertex Medium Working Point (**CSV**) tagger,
1106 described within Section (3.3.2). A cut is placed on the discriminator variable of
1107 > 0.679 , leading to a gluon/light-quark mis-tag rate of 1% and a jet p_T dependant
1108 b-tagging efficiency of 60-70% [64].

1109 Natural **SUSY** models would be characterised through final-state signatures rich
1110 in bottom quarks. A search relying on methods to identify jets originating from
1111 bottom quarks through b-tagging, will significantly improve the sensitivity to this
1112 class of signature.

1113 This is achieved via the binning of events in the signal region according to the
1114 number of b-tagged jets reconstructed in each event, in the following: 0,1,2,3, ≥ 4
1115 b-tag categories . In the highest ≥ 4 b-tag category due to a limited number of
1116 expected signal and background, just three H_T bins are employed: 275-325 GeV,
1117 325-375 GeV, ≥ 375 GeV.

1118 This characterisation is identically mirrored in all control samples, with the infor-
1119 mation from all samples and b-tag categories used simultaneously in the likelihood
1120 model (see Chapter 5) in order to interpret the results in a coherent and powerful
1121 way.

1122 The combination of the H_T , jet multiplicity and b-tag categorisation of the signal
1123 region as described above, resultantly leads to 67 different bins in which the analysis is
1124 interpreted in, which is depicted in Figure 4.4.

1125 4.2.1. Control Sample Definition

1126 The method used to estimate these background contributions in the hadronic signal
1127 region relies on the use of a Transfer Factor (**TF**). This is determined from MC simulation
1128 in both the control and signal region to transform the observed yield measured in data
1129 for a control sample into a background prediction.

1130 The control samples and the **EWK** processes they are specifically tuned to select are
1131 defined as:

1132 **The $\mu +$ jets control sample**

1133 Events from $W +$ jets and $t\bar{t}$

1134 **The $\mu\mu +$ jets control sample**

1135 The

1136 **The $\gamma +$ jets control sample**

1137 The ...

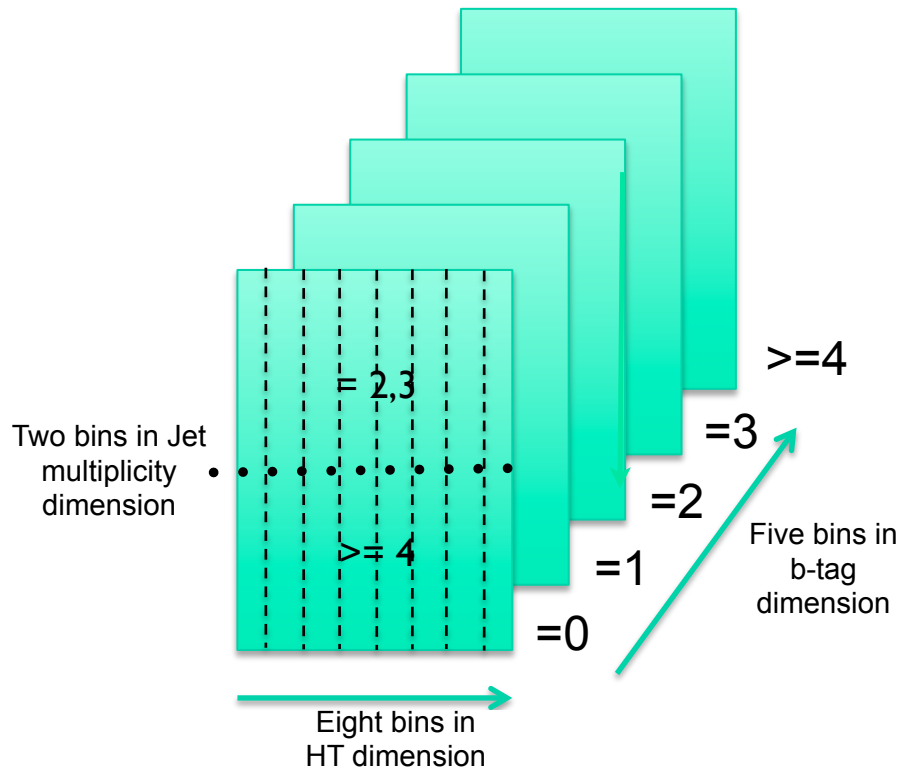


Figure 4.4.: Pictorial depiction of the analysis strategy employed by the α_T search to increase sensitivity to a wide spectra of **SUSY** models.

₁₁₃₈ **4.3. Trigger Strategy**

₁₁₃₉ **4.4. Event Selection**

₁₁₄₀ **4.5. A method to determine MC yields with higher
₁₁₄₁ statistical precision**

₁₁₄₂ **4.6. Systematic Uncertainties on Transfer Factors**

₁₁₄₃ **4.7. Searches for Natural SUSY with B-tag
₁₁₄₄ templates.**

₁₁₄₅ Btag Templates blah blah

Chapter 5.

¹¹⁴⁶ Results

¹¹⁴⁷ Results at 12fb 8TeV

¹¹⁴⁸ 5.1. Statistical Interpretation

¹¹⁴⁹ Likelihood stuff

¹¹⁵⁰ 5.2. Interpretation in Simplified Signal Models

¹¹⁵¹ Result interpretation

¹¹⁵²

Appendix A.

¹¹⁵³ Miscellaneous

¹¹⁵⁴ A.1. Noise Filters

¹¹⁵⁵ For Calo jets the following criteria were applied:

¹¹⁵⁶ • N90 hits > 1 ,

¹¹⁵⁷ • HBHE > 0.01 ,

¹¹⁵⁸ • fHPD < 0.98 ,

¹¹⁵⁹ For PF jets the following criteria were applied:

¹¹⁶⁰ • Neutral hadron fraction < 0.99 ,

¹¹⁶¹ • Neutral EM fraction < 0.99 ,

¹¹⁶² • Number of constituents > 1 ,

¹¹⁶³ • Charged hadron fraction > 0 ,

¹¹⁶⁴ • Charged multiplicity > 0 ,

¹¹⁶⁵ • Charged EM fraction < 0.99 .

¹¹⁶⁶ The following noise filters are applied, to remove events with spurious, non-physical
¹¹⁶⁷ jets or missing transverse energy.

¹¹⁶⁸ • CSC tight beam halo filter,

¹¹⁶⁹ • HBHE noise filter with isolated noise rejection,

- ₁₁₇₀ • HCAL laser filter,
- ₁₁₇₁ • ECAL dead cell trigger primitive (TP) filter,
- ₁₁₇₂ • Tracking failure filter,
- ₁₁₇₃ • Bad EE Supercrystal filter,
- ₁₁₇₄ • ECAL Laser correction filter.

₁₁₇₅ **A.2. Primary Vertices**

₁₁₇₆ The pileup per event is defined by the number of 'good' reconstructed primary vertices
₁₁₇₇ in the event, with each vertex satisfying the following requirements

- ₁₁₇₈ • $N_{dof} > 4$;
- ₁₁₇₉ • vertex position along the bead direction of $|z_{vtx}| < 24\text{cm}$;
- ₁₁₈₀ • vertex position perpendicular to the beam of $\rho < 2\text{cm}$.

Appendix B.

¹¹⁸¹ L1 Jets

¹¹⁸² B.1. Jet matching efficiencies

¹¹⁸³ The single jet turn-on curves are derived from events independent of whether the leading
¹¹⁸⁴ jet in an event is matched to a Level 1 jet using ΔR matching detailed in Section (3.4.3)
¹¹⁸⁵ or not. These turn-ons are produced from events which are not triggered on jet quantities
¹¹⁸⁶ and therefore it is not guaranteed that the lead jet of an event will be seeded by a Level
¹¹⁸⁷ 1 jet. Figure B.1 shows the particular matching efficiency of a lead jet to a L1 jet.

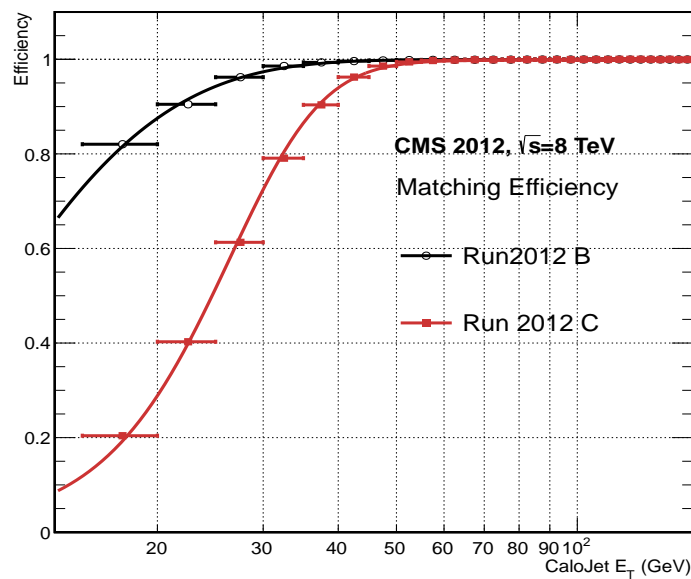


Figure B.1.: Leading jet matching efficiency as a function of the offline CaloJet E_T , measured in an isolated muon triggered dataset in the 2012B and 2012C run periods.

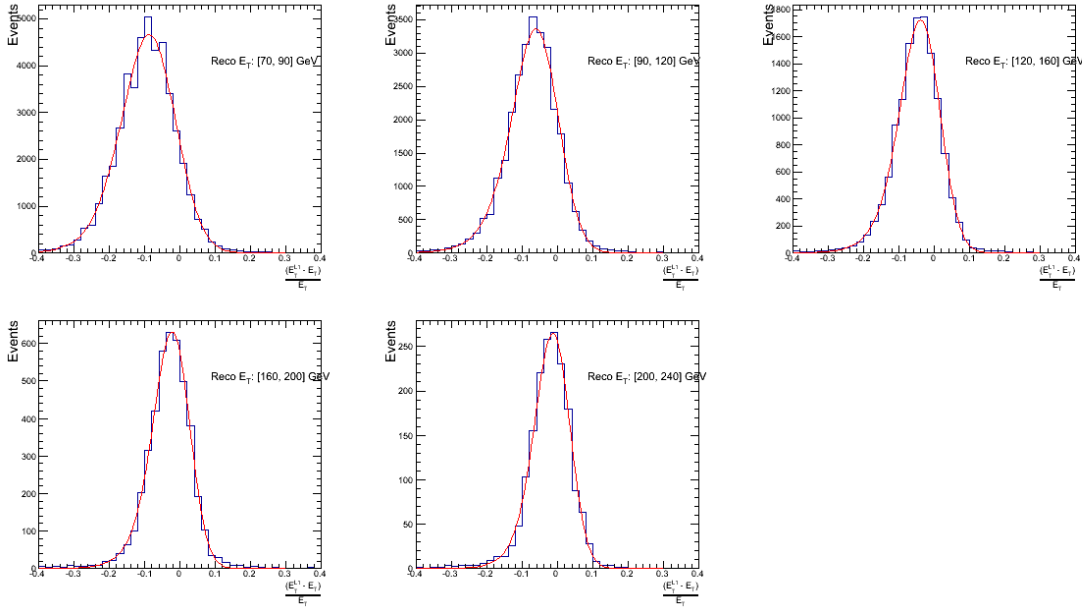
Run Period	μ	σ
2012B	6.62 ± 0.01	0.79 ± 0.03
2012C	19.51 ± 0.03	7.14 ± 0.02

Table B.1.: Results of a cumulative EMG function fit to the turn-on curves for the matching efficiency of the leading jet in an event to a Level-1 jet in run 2012C and 2012B data, measured in an isolated muon triggered sample. The turn-on point, μ , and resolution, σ , are measured with respect to offline Calo Jet E_T .

It can be seen that the turn on is sharper during the 2012B run period. The seed threshold requirement of a 5 GeV jet seed in run 2012C results in more events in which even the lead offline jet does not have an associated L1 jet. For larger jet E_T thresholds, typical of thresholds used in physics analyses, 100% efficiency is observed.

The matching efficiencies have a μ values of 6.62 GeV and 19.51 GeV for Run 2012B and 2012C respectively and is shown in Table B.1.

B.2. Leading Jet Energy Resolution



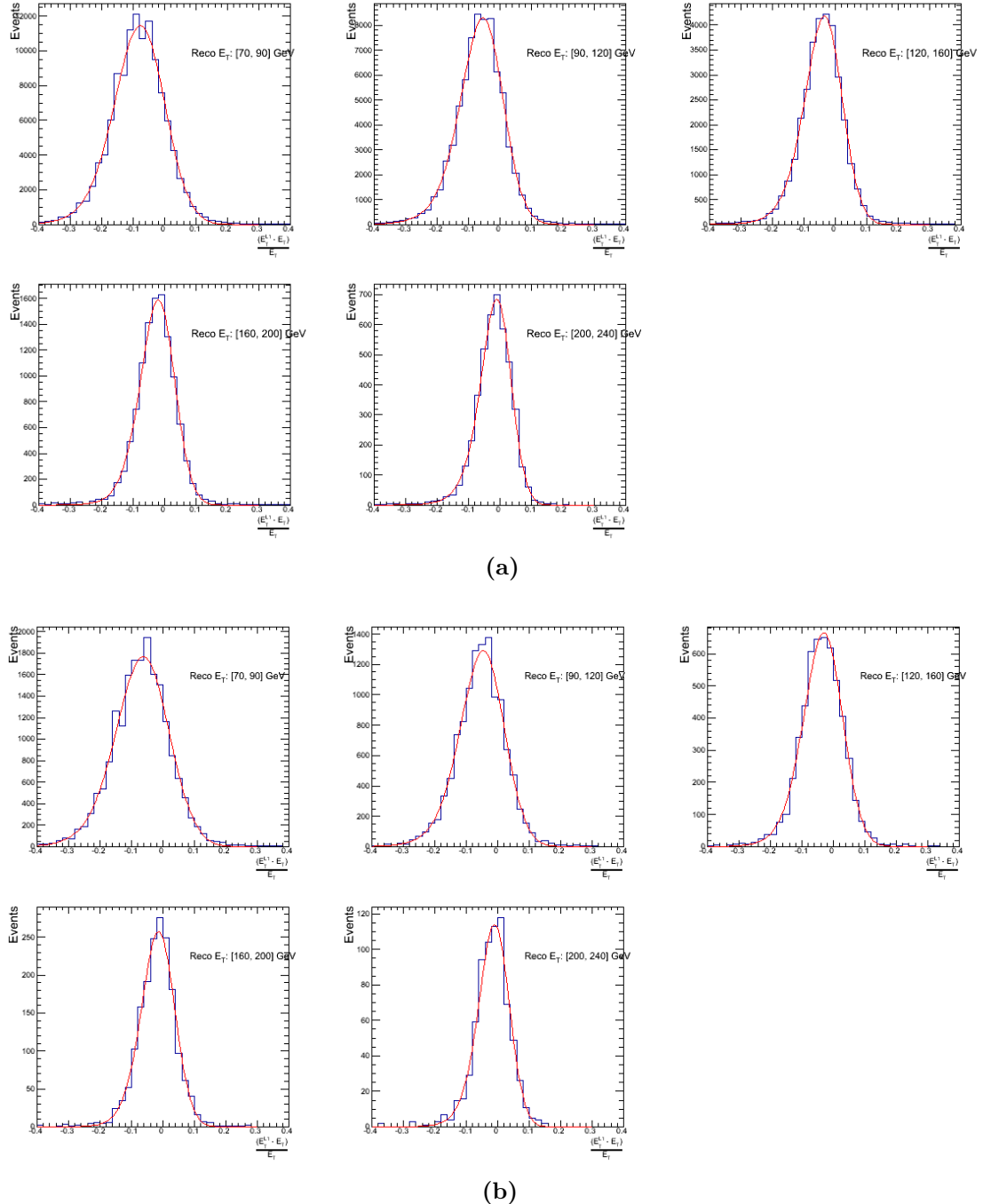
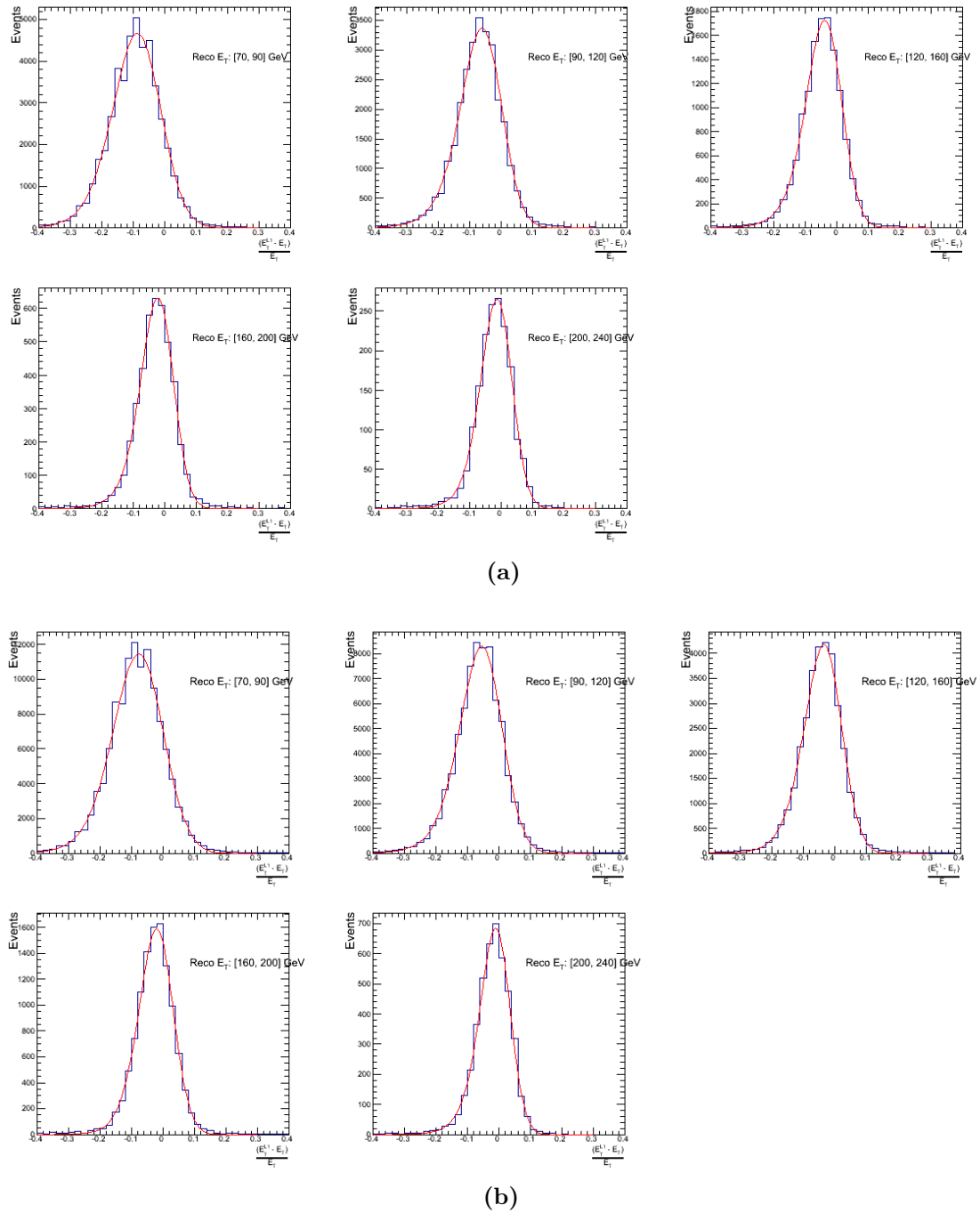
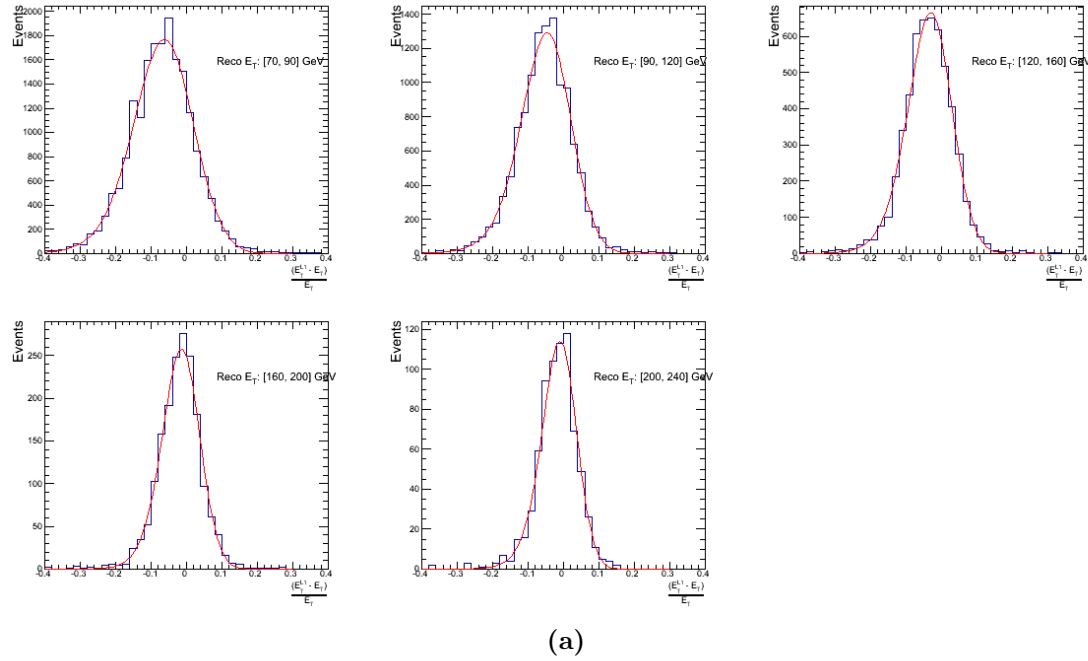


Figure B.2.: Resolution plots of the leading offline jet Calo E_T measured as a function of $\frac{(E_T^{\text{L1}} - E_T^{\text{off}})}{E_T^{\text{off}}}$ for low (a), medium (b) and high (c) pile-up conditions.





(a)

Figure B.3.: Resolution plots of the leading offline jet PF E_T measured as a function of $\frac{(L1 E_T - Offline E_T)}{Offline E_T}$ for low (a), medium (b) and high (c) pile-up conditions.

1195 B.3. Resolution for Energy Sum Quantities

1196 The following plots show the resolution parameters for the four energy sum quantities as
 1197 a function of the quantity (q) itself. In this case, The mean and RMS of the individual
 1198 $\frac{(L1 q - Offline q)}{Offline q}$ distributions, in bins of the quantity q is displayed.

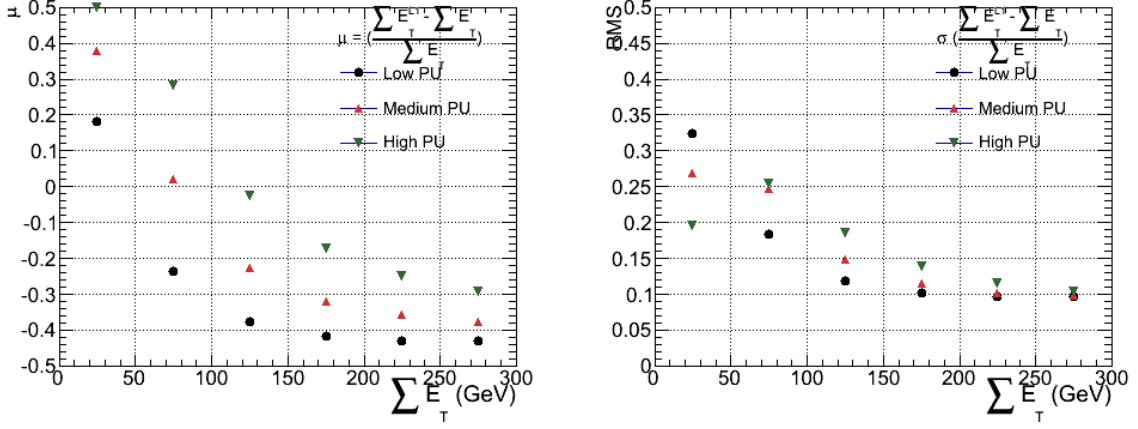


Figure B.4.: $\sum E_T$ resolution parameters in bins of Calo $\sum E_T$ measured for the defined low, medium and high pile up conditions. The plots show the mean μ (left), resolution σ (RMS) of the $\frac{\Delta q}{q}$ distributions.

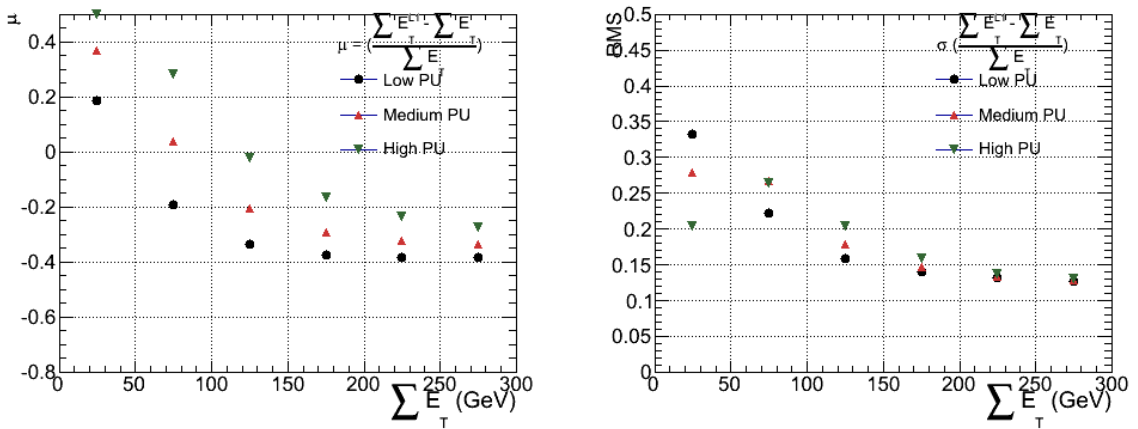


Figure B.5.: $\sum E_T$ resolution parameters in bins of PF $\sum E_T$ measured for the defined low, medium and high pile up conditions. The plots show the mean μ (left), resolution σ (RMS) of the $\frac{\Delta q}{q}$ distributions.

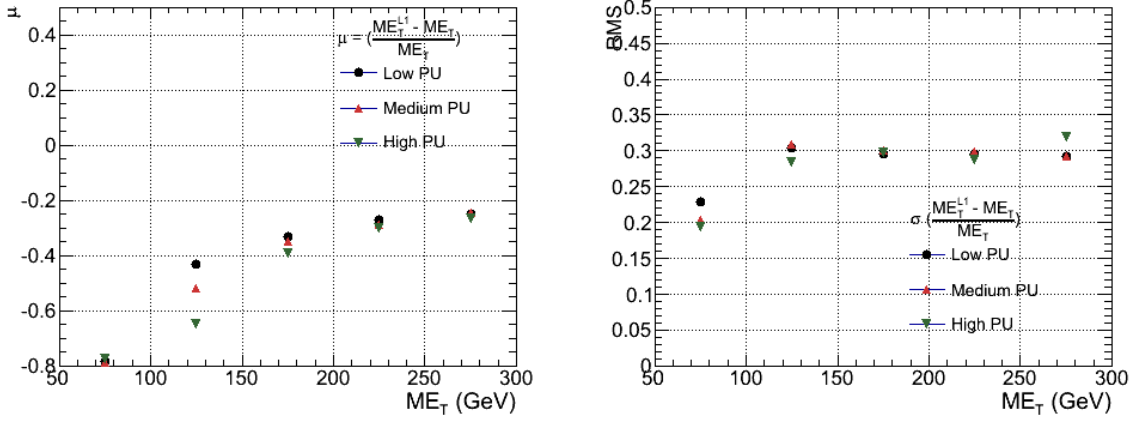


Figure B.6.: \mathcal{E}_T resolution parameters in bins of Calo \mathcal{E}_T measured for the defined low, medium and high pile up conditions. The plots show the mean μ (left), resolution σ (RMS) of the $\frac{\Delta q}{q}$ distributions.

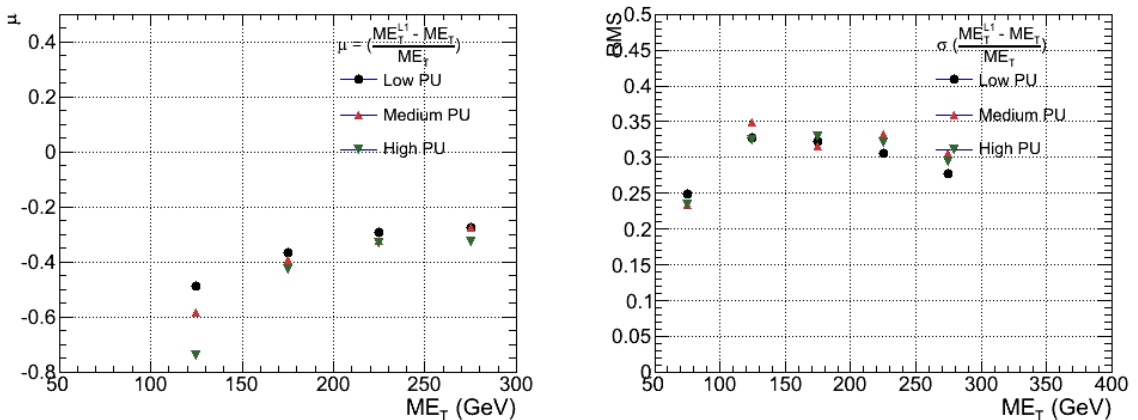


Figure B.7.: \mathcal{E}_T resolution parameters in bins of PF \mathcal{E}_T measured for the defined low, medium and high pile up conditions. The plots show the mean μ (left), resolution σ (RMS) of the $\frac{\Delta q}{q}$ distributions.

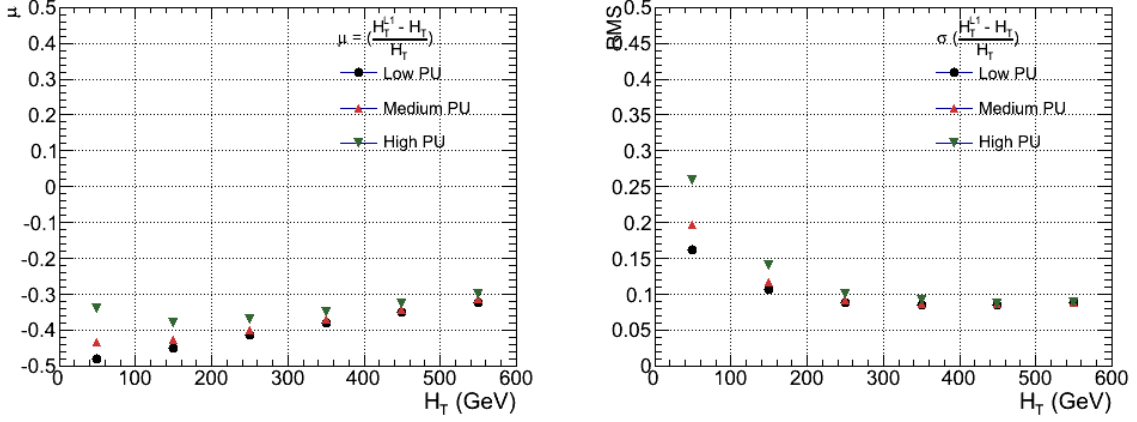


Figure B.8.: H_T resolution parameters in bins of Calo H_T measured for the defined low, medium and high pile up conditions. The plots show the mean μ (left), resolution σ (RMS) of the $\frac{\Delta q}{q}$ distributions.

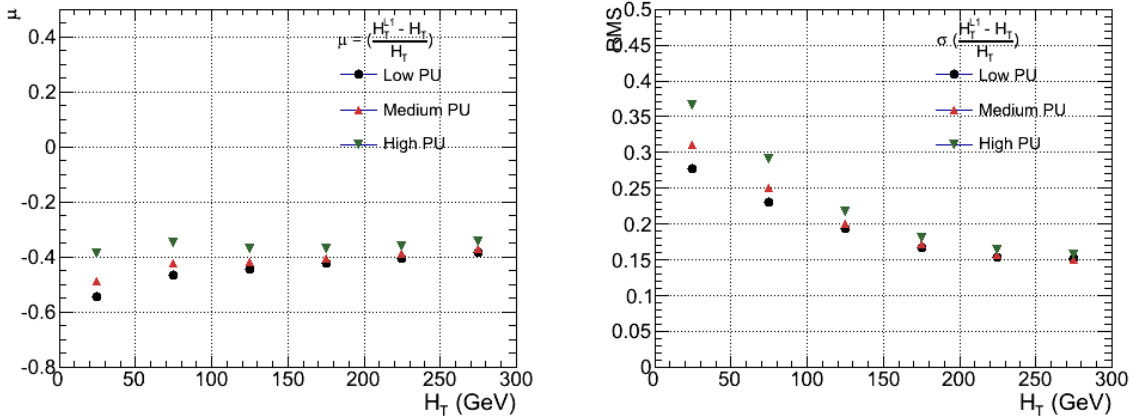


Figure B.9.: H_T resolution parameters in bins of PF H_T measured for the defined low, medium and high pile up conditions. The plots show the mean μ (left), resolution σ (RMS) of the $\frac{\Delta q}{q}$ distributions.

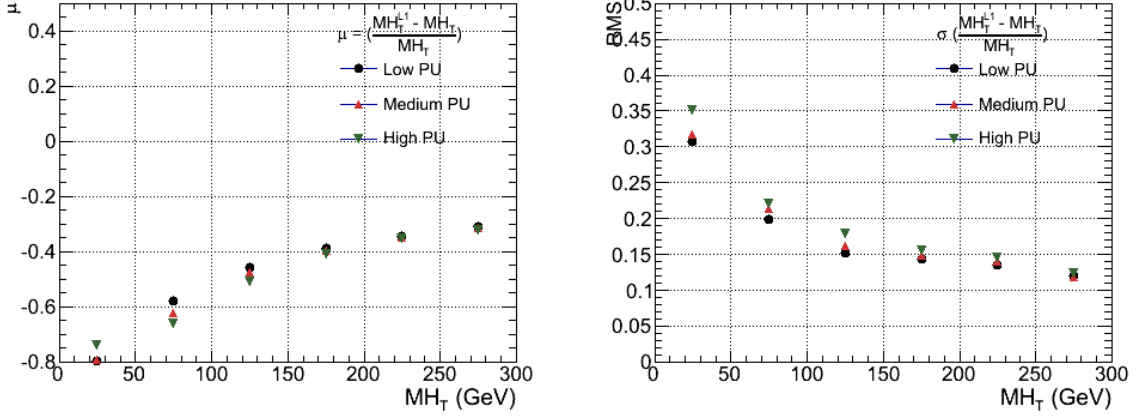


Figure B.10.: H_T resolution parameters in bins of H_T measured for the defined low, medium and high pile up conditions. The plots show the mean μ (left), resolution σ (RMS) of the $\frac{\Delta q}{q}$ distributions.

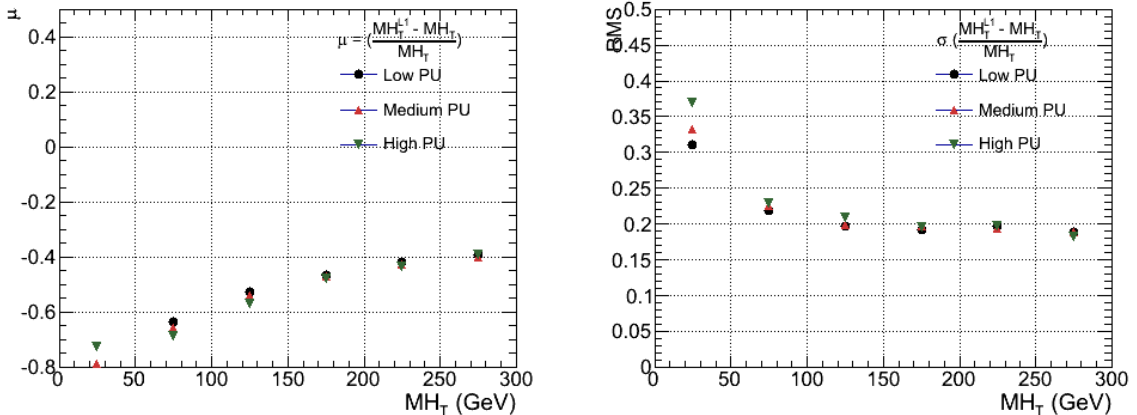


Figure B.11.: H_T resolution parameters in bins of PF H_T measured for the defined low, medium and high pile up conditions. The plots show the mean μ (left), resolution σ (RMS) of the $\frac{\Delta q}{q}$ distributions.

¹²⁰⁰ Bibliography

- ¹²⁰¹ [1] J. Beringer *et al.*, “Review of Particle Physics (RPP),” *Phys.Rev.*, vol. D86, p. 010001, 2012.
- ¹²⁰³ [2] G. H. et al., “Nine-year wilkinson microwave anisotropy probe (wmap) observations: Cosmological parameter results,” *The Astrophysical Journal Supplement Series*, vol. 208, no. 2, p. 19, 2013.
- ¹²⁰⁶ [3] G. Aad *et al.*, “Observation of a new particle in the search for the Standard Model Higgs boson with the ATLAS detector at the LHC,” *Phys.Lett.*, vol. B716, pp. 1–29, 2012.
- ¹²⁰⁹ [4] S. Chatrchyan *et al.*, “Observation of a new boson at a mass of 125 GeV with the CMS experiment at the LHC,” *Phys.Lett.*, vol. B716, pp. 30–61, 2012.
- ¹²¹¹ [5] S. Chatrchyan *et al.*, “Search for supersymmetry in hadronic final states with missing transverse energy using the variables AlphaT and b-quark multiplicity in pp collisions at 8 TeV,” *Eur.Phys.J.*, vol. C73, p. 2568, 2013.
- ¹²¹⁴ [6] S. Weinberg, “A model of leptons,” *Phys. Rev. Lett.*, vol. 19, pp. 1264–1266, Nov 1967.
- ¹²¹⁶ [7] S. Glashow, “Partial Symmetries of Weak Interactions,” *Nucl.Phys.*, vol. 22, pp. 579–588, 1961.
- ¹²¹⁸ [8] A. Salam, “Weak and Electromagnetic Interactions,” *Conf.Proc.*, vol. C680519, pp. 367–377, 1968.
- ¹²²⁰ [9] G. Hooft, “Renormalizable lagrangians for massive yang-mills fields,” *Nuclear Physics B*, vol. 35, no. 1, pp. 167 – 188, 1971.
- ¹²²² [10] F. Hasert *et al.*, “Observation of Neutrino Like Interactions Without Muon Or Electron in the Gargamelle Neutrino Experiment,” *Phys.Lett.*, vol. B46, pp. 138–140, 1973.

- [1225] [11] G. Arnison *et al.*, “Experimental Observation of Lepton Pairs of Invariant Mass
[1226] Around 95-GeV/c**2 at the CERN SPS Collider,” *Phys.Lett.*, vol. B126, pp. 398–410,
[1227] 1983.
- [1228] [12] M. Banner *et al.*, “Observation of Single Isolated Electrons of High Transverse
[1229] Momentum in Events with Missing Transverse Energy at the CERN anti-p p
[1230] Collider,” *Phys.Lett.*, vol. B122, pp. 476–485, 1983.
- [1231] [13] E. Noether, “Invariante variationsprobleme,” *Nachrichten von der Gesellschaft
[1232] der Wissenschaften zu Gttingen, Mathematisch-Physikalische Klasse*, vol. 1918,
[1233] pp. 235–257, 1918.
- [1234] [14] F. Halzen and A. D. Martin, “Quarks and leptons.” Wiley, 1985.
- [1235] [15] *Introduction to Elementary Particles*. Wiley-VCH, 2nd ed., Oct. 2008.
- [1236] [16] C. S. Wu, E. Ambler, R. W. Hayward, D. D. Hoppes, and R. P. Hudson, “Ex-
[1237] perimental Test of Parity Conservation in Beta Decay,” *Physical Review*, vol. 105,
[1238] pp. 1413–1415, Feb. 1957.
- [1239] [17] P. Higgs, “Broken symmetries, massless particles and gauge fields,” *Physics Letters*,
[1240] vol. 12, no. 2, pp. 132 – 133, 1964.
- [1241] [18] F. Englert and R. Brout, “Broken symmetry and the mass of gauge vector mesons,”
[1242] *Phys. Rev. Lett.*, vol. 13, pp. 321–323, Aug 1964.
- [1243] [19] P. W. Higgs, “Broken symmetries and the masses of gauge bosons,” *Phys. Rev. Lett.*,
[1244] vol. 13, pp. 508–509, Oct 1964.
- [1245] [20] G. S. Guralnik, C. R. Hagen, and T. W. B. Kibble, “Global conservation laws and
[1246] massless particles,” *Phys. Rev. Lett.*, vol. 13, pp. 585–587, Nov 1964.
- [1247] [21] S. Weinberg, “A model of leptons,” *Phys. Rev. Lett.*, vol. 19, pp. 1264–1266, Nov
[1248] 1967.
- [1249] [22] H. Yukawa, “On the interaction of elementary particles. i,” *Progress of Theoretical
[1250] Physics Supplement*, vol. 1, pp. 1–10, 1955.
- [1251] [23] Y. e. a. Fukuda, “Evidence for oscillation of atmospheric neutrinos,” *Phys. Rev.
[1252] Lett.*, vol. 81, pp. 1562–1567, Aug 1998.
- [1253] [24] R. Becker-Szendy, C. Bratton, D. Casper, S. Dye, W. Gajewski, *et al.*, “A Search
[1254] for muon-neutrino oscillations with the IMB detector,” *Phys.Rev.Lett.*, vol. 69,

- 1255 pp. 1010–1013, 1992.
- 1256 [25] S. P. Martin, “A Supersymmetry primer,” 1997.
- 1257 [26] H. Nilles, *Supersymmetry, Supergravity and Particle Physics*. Physics reports, North-Holland Physics Publ., 1984.
- 1259 [27] H. E. Haber and G. L. Kane, “The Search for Supersymmetry: Probing Physics Beyond the Standard Model,” *Phys.Rept.*, vol. 117, pp. 75–263, 1985.
- 1261 [28] E. Witten, “Dynamical Breaking of Supersymmetry,” *Nucl.Phys.*, vol. B188, p. 513, 1981.
- 1263 [29] J. Wess and B. Zumino, “Supergauge transformations in four dimensions,” *Nuclear Physics B*, vol. 70, no. 1, pp. 39 – 50, 1974.
- 1265 [30] H. Muller-Kirsten and A. Wiedemann, *Introduction to Supersymmetry*. World Scientific lecture notes in physics, World Scientific, 2010.
- 1267 [31] I. Aitchison, *Supersymmetry in Particle Physics: An Elementary Introduction*. Cambridge University Press, 2007.
- 1269 [32] K. A. Intriligator and N. Seiberg, “Lectures on Supersymmetry Breaking,” *Class.Quant.Grav.*, vol. 24, pp. S741–S772, 2007.
- 1271 [33] Y. Shadmi, “Supersymmetry breaking,” pp. 147–180, 2006.
- 1272 [34] C. Burgess, P. G. Camara, S. de Alwis, S. Giddings, A. Maharana, *et al.*, “Warped Supersymmetry Breaking,” *JHEP*, vol. 0804, p. 053, 2008.
- 1274 [35] H. Murayama, “Supersymmetry breaking made easy, viable, and generic,” 2007.
- 1275 [36] H. Baer and X. Tata, *Weak Scale Supersymmetry: From Superfields to Scattering Events*. Cambridge University Press, 2006.
- 1277 [37] S. P. Martin, “Implications of supersymmetric models with natural r-parity conservation,” 1996.
- 1279 [38] G. L. Kane, C. F. Kolda, L. Roszkowski, and J. D. Wells, “Study of constrained minimal supersymmetry,” *Phys.Rev.*, vol. D49, pp. 6173–6210, 1994.
- 1281 [39] C. Stlege, G. Bertone, D. Cerdeno, M. Fornasa, R. Ruiz de Austri, *et al.*, “Updated global fits of the cmSSM including the latest LHC SUSY and Higgs searches and XENON100 data,” *JCAP*, vol. 1203, p. 030, 2012.

- 1284 [40] M. Citron, J. Ellis, F. Luo, J. Marrouche, K. Olive, *et al.*, “The End of the CMSSM
1285 Coannihilation Strip is Nigh,” *Phys.Rev.*, vol. D87, p. 036012, 2013.
- 1286 [41] D. Ghosh, M. Guchait, S. Raychaudhuri, and D. Sengupta, “How Constrained is
1287 the cMSSM?,” *Phys.Rev.*, vol. D86, p. 055007, 2012.
- 1288 [42] D. Alves *et al.*, “Simplified Models for LHC New Physics Searches,” *J.Phys.*, vol. G39,
1289 p. 105005, 2012.
- 1290 [43] J. Alwall, P. Schuster, and N. Toro, “Simplified Models for a First Characterization
1291 of New Physics at the LHC,” *Phys.Rev.*, vol. D79, p. 075020, 2009.
- 1292 [44] S. Chatrchyan *et al.*, “Interpretation of Searches for Supersymmetry with simplified
1293 Models,” *Phys.Rev.*, vol. D88, p. 052017, 2013.
- 1294 [45] J. Hisano, K. Kurosawa, and Y. Nomura, “Natural effective supersymmetry,”
1295 *Nucl.Phys.*, vol. B584, pp. 3–45, 2000.
- 1296 [46] M. Papucci, J. T. Ruderman, and A. Weiler, “Natural SUSY Endures,” *JHEP*,
1297 vol. 1209, p. 035, 2012.
- 1298 [47] B. Allanach and B. Gripaios, “Hide and Seek With Natural Supersymmetry at the
1299 LHC,” *JHEP*, vol. 1205, p. 062, 2012.
- 1300 [48] K. Aamodt *et al.*, “The ALICE experiment at the CERN LHC,” *JINST*, vol. 3,
1301 p. S08002, 2008.
- 1302 [49] G. Aad *et al.*, “The ATLAS Experiment at the CERN Large Hadron Collider,”
1303 *JINST*, vol. 3, 2008.
- 1304 [50] R. Adolphi *et al.*, “The cms experiment at the cern lhc,” *JINST*, vol. 0803, p. S08004,
1305 2008.
- 1306 [51] A. A. Alves *et al.*, “The LHCb Detector at the LHC,” *JINST*, vol. 3, p. S08005,
1307 2008.
- 1308 [52] J.-L. Caron, “Lhc layout.. schema general du lhc..” Sep 1997.
- 1309 [53] C. Collaboration, “Cms luminosity - public results.”
1310 twiki.cern.ch/twiki/bin/view/CMSPublic/LumiPublicResults., 2011.
- 1311 [54] CERN, “Cms compact muon solenoid..” <http://public.web.cern.ch/public/Objects/LHC/CMSnc.jpg>
1312 Feb 2010.

- 1313 [55] *The CMS electromagnetic calorimeter project: Technical Design Report*. Technical
1314 Design Report CMS, Geneva: CERN, 1997.
- 1315 [56] *The CMS muon project: Technical Design Report*. Technical Design Report CMS,
1316 Geneva: CERN, 1997.
- 1317 [57] CMS Collaboration, “The cms physics technical design report, volume 1,”
1318 *CERN/LHCC*, vol. 2006-001, 2006.
- 1319 [58] M. Cacciari, G. P. Salam, and G. Soyez, “The anti- k_t jet clustering algorithm,”
1320 *Journal of High Energy Physics*, vol. 2008, no. 04, p. 063, 2008.
- 1321 [59] “Jet performance in pp collisions at 7 tev,” Tech. Rep. CMS-PAS-JME-10-003,
1322 CERN, Geneva, 2010.
- 1323 [60] X. Janssen, “Underlying event and jet reconstruction in cms,” Tech. Rep. CMS-CR-
1324 2011-012, CERN, Geneva, Jan 2011.
- 1325 [61] T. C. collaboration, “Determination of jet energy calibration and transverse mo-
1326 mentum resolution in cms,” *Journal of Instrumentation*, vol. 6, no. 11, p. P11002,
1327 2011.
- 1328 [62] R. Eusebi and on behalf of the CMS collaboration), “Jet energy corrections and
1329 uncertainties in cms: reducing their impact on physics measurements,” *Journal of
1330 Physics: Conference Series*, vol. 404, no. 1, p. 012014, 2012.
- 1331 [63] “Algorithms for b Jet identification in CMS,” Tech. Rep. CMS-PAS-BTV-09-001,
1332 CERN, 2009. Geneva, Jul 2009.
- 1333 [64] “Performance of b tagging at $\sqrt{s}=8$ tev in multijet, ttbar and boosted topology
1334 events,” no. CMS-PAS-BTV-13-001, 2013.
- 1335 [65] T. C. collaboration, “Identification of b-quark jets with the cms experiment,” *Journal
1336 of Instrumentation*, vol. 8, no. 04, p. P04013, 2013.
- 1337 [66] S. Dasu *et al.*, “CMS. The TriDAS project. Technical design report, vol. 1: The
1338 trigger systems,” 2000.
- 1339 [67] P. Sphicas, “CMS: The TriDAS project. Technical design report, Vol. 2: Data
1340 acquisition and high-level trigger,” 2002.
- 1341 [68] J. B. et al., “Calibration and Performance of the Jets and Energy Sums in the
1342 Level-1 Trigger ,” no. CMS IN 2013/006 (2013), 2013.

- ₁₃₄₃ [69] B. et al., “Study of Level-1 Trigger Jet Performance in High Pile-up Running
₁₃₄₄ Conditions,” no. CMS IN 2013/007 (2013), 2013.
- ₁₃₄₅ [70] J. J. Brooke, “Performance of the cms level-1 trigger,” Tech. Rep. CMS-CR-2012-322.
₁₃₄₆ CERN-CMS-CR-2012-322, CERN, Geneva, Nov 2012.
- ₁₃₄₇ [71] L. Randall and D. Tucker-Smith, “Dijet searches for supersymmetry at the large
₁₃₄₈ hadron collider,” *Phys. Rev. Lett.*, vol. 101, p. 221803, Nov 2008.
- ₁₃₄₉ [72] “SUSY searches with dijet events,” 2008.
- ₁₃₅₀ [73] “Search strategy for exclusive multi-jet events from supersymmetry at CMS,” Tech.
₁₃₅₁ Rep. CMS-PAS-SUS-09-001, CERN, 2009. Geneva, Jul 2009.

1352 Acronyms

1353	ALICE	A Large Ion Collider Experiment
1354	ATLAS	A Toroidal LHC ApparatuS
1355	APD	Avalanche Photo-Diodes
1356	BSM	Beyond Standard Model
1357	CERN	European Organization for Nuclear Research
1358	CMS	Compact Muon Solenoid
1359	CMSSM	Compressed Minimal SuperSymmetric Model
1360	CSC	Cathode Stripe Chamber
1361	CSV	Combined Secondary Vertex
1362	CSVM	Combined Secondary Vertex Medium Working Point
1363	DT	Drift Tube
1364	ECAL	Electromagnetic CALorimeter
1365	EB	Electromagnetic CALorimeter Barrel
1366	EE	Electromagnetic CALorimeter Endcap
1367	ES	Electromagnetic CALorimeter pre-Shower
1368	EMG	Exponentially Modified Gaussian
1369	EPJC	European Physical Journal C
1370	EWK	Electroweak Sector
1371	GCT	Global Calorimeter Trigger
1372	GMT	Global MuonTrigger
1373	GT	Global Trigger
1374	HB	Hadron Barrel
1375	HE	Hadron Endcaps

1376	HF	Hadron Forward
1377	HO	Hadron Outer
1378	HCAL	Hadronic CALorimeter
1379	HLT	Higher Level Trigger
1380	LUT	Look Up Table
1381	L1	Level 1 Trigger
1382	LHC	Large Hadron Collider
1383	LHCb	Large Hadron Collider Beauty
1384	LSP	Lightest Supersymmetric Partner
1385	PS	Proton Synchrotron
1386	QED	Quantum Electro-Dynamics
1387	QCD	Quantum Chromo-Dynamics
1388	QFT	Quantum Field Theory
1389	RPC	Resistive Plate Chamber
1390	RCT	Regional Calorimeter Trigger
1391	RMT	Regional Muon Trigger
1392	SUSY	SUperSYmmetry
1393	SM	Standard Model
1394	SMS	Simplified Model Spectra
1395	SPS	Super Proton Synchrotron
1396	TF	Transfer Factor
1397	VEV	Vacuum Expectation Value
1398	VPT	Vacuum Photo-Triodes
1399	WIMP	Weakly Interacting Massive Particle